# The mechanics of the Gentle Driving of Piles

Tsetas, Athanasios; Tsouvalas, Apostolos; Metrikine, Andrei V.

**DOI**
10.1016/j.ijsolstr.2023.112466

**Publication date**
2023

**Document Version**
Final published version

**Published in**
International Journal of Solids and Structures

International Journal of Solids and Structures 282 (2023) 112466

Contents lists available at ScienceDirect

International Journal of Solids and Structures

journal homepage: www.elsevier.com/locate/ijsolstr

# The mechanics of the Gentle Driving of Piles

Athanasios Tsetas *, Apostolos Tsouvalas, Andrei V. Metrikine

*Faculty of Civil Engineering and Geosciences, Delft University of Technology, Stevinweg 1, Delft, 2628 CN, The Netherlands*

ARTICLE INFO

*Keywords:*
Pile driving
Gentle Driving of Piles
Soil–structure interaction
Friction redirection
Vibrations of shells
Thin-Layer Method
Harmonic Balance Method
Green's functions
Field tests

ABSTRACT

Gentle Driving of Piles (GDP) is a new vibratory installation technology for tubular (mono)piles. It is characterized by the simultaneous application of low-frequency axial and high-frequency torsional vibrations, envisaged to achieve both high installation performance and reduced underwater noise emissions. The concept of GDP has been demonstrated experimentally in a medium-scale onshore field campaign, showcasing the potential of the method in terms of installation and post-installation performances. To further comprehend the mechanics of the GDP method, the driving process is studied by means of a novel pile–soil model; this framework has been recently developed and successfully applied to the problem of axial vibratory driving. In particular, the pile is treated as a thin cylindrical shell via a Semi-analytical Finite Element (SAFE) approach and a linear elastic layered soil half-space is considered via the Thin-Layer Method (TLM) coupled with Perfectly Matched Layers (PMLs). The pile–soil coupling is realized through a hereditary frictional interface and an elasto-plastic tip formulation, both characterized by standard geotechnical *in-situ* measurements. The comparison of numerical results with field data is favourable for drivability purposes, showcasing the potential of the numerical framework for the analysis of GDP. Conclusively, the mechanics of the installation process are deciphered and the redirection of the friction force vector – induced by high-frequency torsion – is identified as the main driving mechanism of GDP.

## 1. Introduction

The acceleration of the global energy transition has led to a remarkable increase in the demand for renewable energy resources (International Energy Agency, 2022). Among these resources, offshore wind energy has emerged as a particularly promising option, given its abundance and cost-effectiveness (Ramírez et al., 2021). To accommodate the international set targets, the technological developments in the area need to expedite, engendering a multitude of engineering challenges (Bilgili and Alphan, 2022). The installation of foundations for offshore wind turbines (OWTs) constitutes one of the most crucial, challenging and costly operations during the construction of an offshore wind farm (Guo et al., 2022).

At present, monopiles comprise the vast majority of offshore wind foundations and the foremost monopile installation method is impact hammering (Merchant, 2019; Musial et al., 2022). Notwithstanding the robustness and efficacy of this technique, alarming environmental concerns have been raised in view of the high levels of underwater noise pollution during installation (Tsouvalas, 2020). Specifically, the hammer impacts on the pile head induce high levels of impulsive noise that pose great harm to marine life (Ainslie et al., 2020). It is vital to realize the ambitious goals of the offshore wind sector in a socially and environmentally responsible manner, thereby the development of sustainable methods for monopile installation is of utmost significance (Williams et al., 2022).

A major candidate among the environmentally friendly alternatives for monopile installation is the vibratory driving technology. In this method, the pile penetration is achieved through the application of axial vibrations at the pile head, resulting from the counter-rotation of eccentric masses. Vibratory pile driving has been employed in onshore projects for almost a century and is associated with quiet(er)/fast installation (Barkan, 1967; Rodger and Littlejohn, 1980; Tsouvalas and Metrikine, 2016). However, the adoption of vibratory driving in offshore monopile installation remains limited to date. The lack of a complete body of field observations and the knowledge gaps in the topic hinder its wider use. Specifically, open research questions need to be addressed, pertaining to the energy efficiency during driving (Gómez et al., 2022), the post-installation stiffness and response to lateral loading (Tsetas et al., 2020; Kementzetzidis et al., 2023b), as well as the installation process itself (Mazza and Holeyman, 2019).

Vibratory pile installation modelling has drawn increasing attention, with advances ranging from engineering-oriented (Kaynia et al., 2022; Xiao and Ge, 2022) to high-fidelity approaches (Staubach et al.,

* Corresponding author.
*E-mail address:* a.tsetas@tudelft.nl (A. Tsetas).

https://doi.org/10.1016/j.ijsolstr.2023.112466
Received 19 May 2023; Received in revised form 15 August 2023; Accepted 21 August 2023
Available online 23 August 2023


(a) (b)

**Fig. 1.** (a) The test site of the GDP field campaign and (b) the GDP shaker at the manufacturing site.

**Table 1**
Technical specifications of the GDP shaker.

| | GDP shaker | |
|---|---|---|
| | Axial shaker | Torsional shaker |
| Total mass [kg] | 5150 | |
| Eccentric moment *me* [kg m] | 15 | 4 |
| Rotational speed [rpm] | 1400 | 4800 |
| Operational power [kW] | 72 | 188 |

2021; Machaček et al., 2021). Customarily, drivability predictions are necessary to assess the capability of a driving device to install a pile up to the target penetration depth, as well as to anticipate and prevent occurrences of high operational risk, e.g. early pile refusal or pile running. Focusing on engineering practice and design, a number of commercial software packages are available for the analysis of (mostly) impact piling and vibratory driving (e.g. ALLWAVE, GRLWEAP and TNOWAVE). At present, the role of pile installation modelling cannot be overemphasized as – next to the previous items – it directly affects the vibro-acoustic and post-installation performances, pointing towards the development of integrated approaches in the future.

With a view to enhance the classical vibratory technique, the Gentle Driving of Piles (GDP) method has been recently proposed and demonstrated experimentally (Tsetas et al., 2023a). GDP aims to enhance the installation performance and reduce the underwater noise emissions during monopile installation, through the simultaneous application of low-frequency axial and high-frequency torsional vibrations. For that purpose, a field tests campaign was conducted and the main experimental findings showcased the potential of the GDP method in terms of installation performance (Tsetas et al., 2023a) and response to lateral loading (Kementzetzidis et al., 2023a). Numerical modelling work is the following necessary step in order to further analyse and interpret the field observations. In that manner, a first set of experimental and numerical works that focus on GDP may be complete. However, none of the previously stated approaches is suitable for this purpose, namely the analysis of pile installation via GDP. To achieve the preceding goals, the development of a numerical modelling framework for GDP constitutes one of the foremost objectives in this research line.

In this paper, the GDP method is studied with a view to comprehend the main driving mechanism and study further the mechanics of the installation process. For that purpose, a numerical model for vibratory pile driving – recently developed and validated against field data – is employed as basis and extended further to analyse pile installation via GDP (Tsetas et al., 2023b). In particular, the pile is described as a thin cylindrical shell via the Semi-analytical Finite Element (SAFE) method, whereas the soil medium comprises a layered soil half-space modelled via the Thin-Layer Method (TLM) (Kausel, 1981), coupled with Perfectly Matched Layers (PMLs) (de Oliveira Barbosa et al., 2012). The pile–soil coupling is realized through a hereditary frictional interface based on Coulomb friction and an elasto-plastic tip formulation; the numerical solution is reached through a sequential scheme that utilizes the Harmonic Balance Method (HBM) (Krack and Gross, 2019). By means of this development, the main novel contribution of this work is realized, namely deciphering the mechanics of the GDP method and the advantageous effect of torsion in vibro-driving. The comparison between numerical results and field data showcases the model validity for drivability purposes and further study of installation aspects is pursued. The redirection of the friction force vector emerges as the major driving mechanism of GDP, as it enhances installation performance by greatly reducing the soil reaction along the penetration axis. Conclusively, a study of the soil motion elicited by GDP demonstrates that the SH wavefield becomes dominant in terms of overall disturbance, whereas the SV-P wavefield is greatly abated.

## 2. Pile installation via axial and torsional vibrations: the Gentle Driving of Piles (GDP) method

The primary objective of the GDP technology is to enhance the axial vibratory driving of piles by introducing high-frequency torsional vibrations alongside low-frequency axial vibrations. The primary motivation of GDP lies in the mobilization of frictional soil reaction along the shaft in the circumferential direction, thereby reducing the vertical shaft reaction that opposes the pile penetration. In particular, the shaft reaction as a friction force is collinear with the vector of relative velocity between pile and soil. The introduction of high-frequency torsion (compared to the axial loading) will lead to high circumferential velocity, thus allocating friction to the circumferential direction and reducing the friction force along the vertical axis. Subsequently, this leads to a reduction in axial driving loads as compared to axial vibro-driving, which results in a decrease in pile radial motion (Poisson effect) (De Nicola and Randolph, 1993; Tsetas et al., 2021). It is noted that torsional excitation, under the assumption of axisymmetric conditions, does not induce radial motion in the pile (Forsberg, 1969). Furthermore, this type of excitation elicits solely SH waves in the surrounding medium (Kausel, 2006), which do not propagate in the seawater (Jensen et al., 2011). In light of these considerations, we postulate that GDP can effectively reduce the underwater noise emissions and enhance the driving performance.

To test the hypothesis of the GDP method, an experimental programme was designed and executed at Maasvlakte II in the Port of

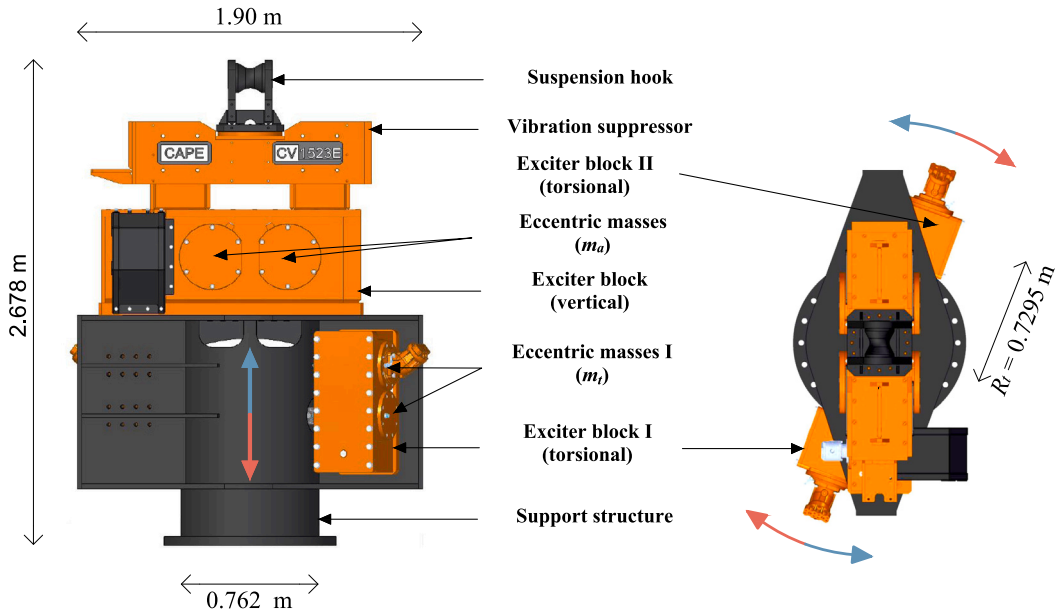


**Fig. 2.** Detailed design of the GDP shaker.

Rotterdam (see Fig. 1(a)). For that purpose, the first phase of this campaign was centred on the development of a pile driving apparatus that could generate the envisaged excitation, namely the GDP shaker (see Fig. 1(b)). In particular, the main technical specifications of the GDP shaker can be found in Table 1 and a detailed view of the apparatus design is shown in Fig. 2. In these tests, the GDP method was compared with standard driving techniques on the basis of installation and lateral loading tests. The main experimental findings, pertaining to the installation and post-installation performances of the GDP piles, are summarized as follows:

– the comparison between GDP and axial vibro-driving showcased the potential of the GDP method, as GDP enabled faster installation in stiffer soil with comparable total energy consumption (Gómez et al., 2022; Tsetas et al., 2023a).

– *in-situ* measurements in the pile vicinity presented an increase of P-wave velocity after installation via GDP, associated with soil stiffness increase due to densification (Tsetas et al., 2023a).

– response to lateral loading did not indicate any compromise of the post-installation performance due to GDP; on the contrary, GDP piles experienced lower displacements during lateral loading compared to the piles driven by impact hammering and axial vibro-driving (Kementzetzidis et al., 2023a).

The experimental tests highlighted the potential of the GDP method and encouraged the development of the technology. To further interpret and complement the GDP experiments, numerical modelling is required and a suitable approach for the analysis of pile installation via GDP is not yet available.

## 3. A numerical model for pile installation via the GDP method

In the ensuing, a numerical model is presented for pile installation via GDP (see Fig. 3). The GDP shaker is considered to be connected at the pile top with a stiff connection along the pile circumference. Accordingly, it is assumed that this connection ensures a uniform distribution of the input excitation – combined vertical and torsional loading – along the circumference. Thereby, the problem of pile installation via GDP is assumed to be axisymmetric, considering that all the components of our model are symmetric around the vertical axis, i.e. pile, soil and input excitation (both axial and torsional). Subsequently, a 3-D axisymmetric pile–soil model – developed for axial vibratory driving and benchmarked with field data – is utilized as a basis and extended further (Tsetas et al., 2023b). By the introduction of the circumferential motion component in both pile and soil, as well as the reformulation of the soil reaction, the GDP method can be analysed.

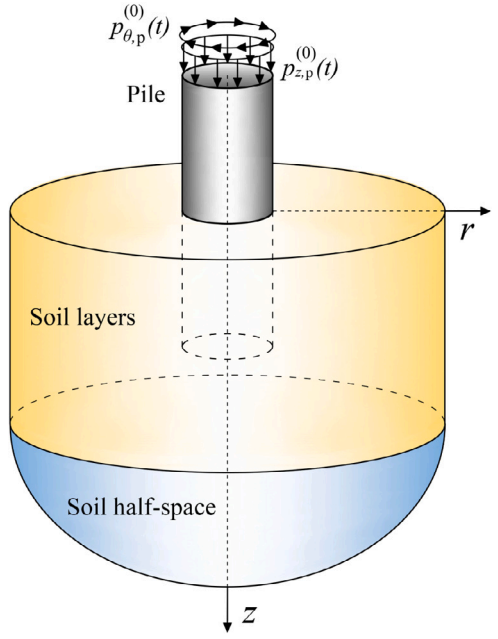


**Fig. 3.** A pipe pile installed in a layered soil medium via vertical and torsional loading.

### 3.1. A Semi-analytical Finite Element (SAFE) model for thin cylindrical shells

A tubular pile is considered with wall thickness $h_p$, length $L_p$ and mid-surface radius $R_p$. The pile material is linear elastic and isotropic with Young's modulus $E_p$, Poisson's ratio $\nu_p$ and mass density $\rho_p$. The pile is treated as a thin cylindrical shell according to the Love–Timoshenko theory (Love, 1888, 1944; Timoshenko and Woinowsky-Krieger, 1959) and its numerical implementation is based on the Semi-analytical Finite Element (SAFE) method (Tsetas et al.,

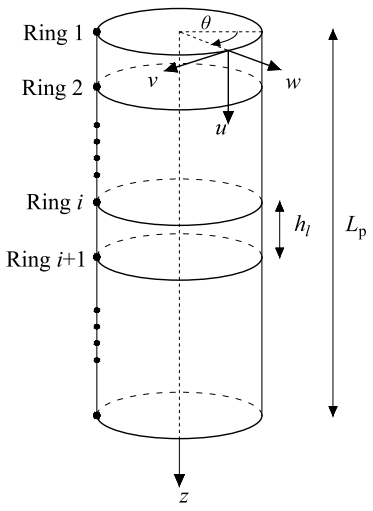


**Fig. 4.** A thin cylindrical shell discretized axially into nodal rings based on the SAFE method.

2023b). Similar approaches have been utilized in the numerical treatment of cylindrical waveguides and plates (Bandyopadhyay and Archer, 1979; Taciroglu et al., 2004; Ahmad and Gabbert, 2012). In the present model, a Finite Element (FE) discretization is considered along the shell longitudinal axis $z$ and the circumferential dependence of the solution is expressed analytically in terms of Fourier series, resulting into a set of nodal rings (see Fig. 4). Accordingly, the general solution of the displacement/rotation vector $\mathbf{u}_\mathrm{p}$ at the nodal rings can be written as:

$$\mathbf{u}_\mathrm{p} = \begin{bmatrix} \mathbf{u} \\ \mathbf{v} \\ \mathbf{w} \\ \boldsymbol{\beta}_z \end{bmatrix} = \sum_{n=0}^{\infty} \left[ \left( \boldsymbol{\Theta}_n^\mathrm{s} \otimes \mathbf{I}_{N_l} \right) \mathbf{u}_{\mathrm{p},n}^\mathrm{s} + \left( \boldsymbol{\Theta}_n^\mathrm{a} \otimes \mathbf{I}_{N_l} \right) \mathbf{u}_{\mathrm{p},n}^\mathrm{a} \right] \tag{1}$$

where $\mathbf{u}$, $\mathbf{v}$, $\mathbf{w}$, $\boldsymbol{\beta}_z$ are the vectors of the respective displacement/rotation values at the nodal rings, $n$ is the circumferential mode number, $\otimes$ is the Kronecker product and $\mathbf{I}_{N_l}$ is the $N_l \times N_l$ identity matrix with $N_l$ being the number of nodal rings. The diagonal matrices $\boldsymbol{\Theta}_n^\mathrm{s}$ and $\boldsymbol{\Theta}_n^\mathrm{a}$ ensure that the response is periodic in $\theta$:

$$\begin{aligned} \boldsymbol{\Theta}_n^\mathrm{s} &= \mathrm{diag}\left\{ \cos(n\theta) \quad -\sin(n\theta) \quad \cos(n\theta) \quad \cos(n\theta) \right\}, \\ \boldsymbol{\Theta}_n^\mathrm{a} &= \mathrm{diag}\left\{ \sin(n\theta) \quad \cos(n\theta) \quad \sin(n\theta) \quad \sin(n\theta) \right\} \end{aligned} \tag{2}$$

where the superscripts $(\cdot)^\mathrm{s}$ and $(\cdot)^\mathrm{a}$ denote the symmetric and anti-symmetric azimuthal configurations with respect to $\theta = 0$. It follows that the vectors $\mathbf{u}_{\mathrm{p},n}^\mathrm{s}$ and $\mathbf{u}_{\mathrm{p},n}^\mathrm{a}$ are the associated azimuthal components of the nodal displacement/rotation vectors. More details on the derivation of the SAFE model for thin cylindrical shells can be found in Tsetas et al. (2023b) and Tsetas (2023).

Similarly to axial vibratory driving, the GDP model is also considered axisymmetric, i.e. $n = 0$. Furthermore, both axial and circumferential vibrations are applied (from the GDP shaker) at the pile top, thus exciting both the axial–radial and the circumferential types of axisymmetric shell motion (Callahan and Baruh, 1999); these correspond to the symmetric and anti-symmetric configurations for $n = 0$, respectively (Tsetas et al., 2023b). The axial–radial shell response is governed by the following equations of motion:

$$\mathbf{I}_{\mathrm{p},0}^\mathrm{s} \frac{\mathrm{d}^2 \mathbf{u}_{\mathrm{p},0}^\mathrm{s}}{\mathrm{d}t^2} + \mathbf{L}_{\mathrm{p},0}^\mathrm{s} \mathbf{u}_{\mathrm{p},0}^\mathrm{s} = \mathbf{p}_{\mathrm{p},0}^\mathrm{s} \tag{3}$$

whereas the SAFE equations of motion that describe the purely circumferential motion read:

$$\mathbf{I}_{\mathrm{p},0}^\mathrm{a} \frac{\mathrm{d}^2 \mathbf{u}_{\mathrm{p},0}^\mathrm{a}}{\mathrm{d}t^2} + \mathbf{L}_{\mathrm{p},0}^\mathrm{a} \mathbf{u}_{\mathrm{p},0}^\mathrm{a} = \mathbf{p}_{\mathrm{p},0}^\mathrm{a} \tag{4}$$

where $\mathbf{I}_{\mathrm{p},0}^\mathrm{s}$, $\mathbf{I}_{\mathrm{p},0}^\mathrm{a}$ are the SAFE shell mass matrices and $\mathbf{L}_{\mathrm{p},0}^\mathrm{s}$ $\mathbf{L}_{\mathrm{p},0}^\mathrm{a}$ are the SAFE shell stiffness matrices; the SAFE matrices for a cylindrical shell element are given in Appendix A. The displacement/rotation vectors at the nodal rings $\mathbf{u}_{\mathrm{p},0}^\mathrm{s}$, $\mathbf{u}_{\mathrm{p},0}^\mathrm{a}$ may be expressed as:

$$\mathbf{u}_{\mathrm{p},0}^\mathrm{s} = \begin{bmatrix} \mathbf{u}_0^\mathrm{s} \\ \mathbf{w}_0^\mathrm{s} \\ \boldsymbol{\beta}_{z,0}^\mathrm{s} \end{bmatrix}, \quad \mathbf{u}_{\mathrm{p},0}^\mathrm{a} = \mathbf{v}_0^\mathrm{a} \tag{5}$$

In similar fashion, the vectors of consistent forces/moments at the nodal rings are denoted as $\mathbf{p}_{\mathrm{p},0}^\mathrm{s}$, $\mathbf{p}_{\mathrm{p},0}^\mathrm{a}$ and read:

$$\mathbf{p}_{\mathrm{p},0}^\mathrm{s} = \begin{bmatrix} \mathbf{p}_{z0,\mathrm{p}}^\mathrm{s} \\ \mathbf{p}_{r0,\mathrm{p}}^\mathrm{s} \\ \mathbf{m}_{zz0,\mathrm{p}}^\mathrm{s} \end{bmatrix}, \quad \mathbf{p}_{\mathrm{p},0}^\mathrm{a} = \mathbf{p}_{\theta 0,\mathrm{p}}^\mathrm{a} \tag{6}$$

It is remarked that $\mathbf{p}_{\mathrm{p},0}^\mathrm{s}$ and $\mathbf{p}_{\mathrm{p},0}^\mathrm{a}$ also encompass the non-linear pile–soil interaction loads, with a view to the full pile driving model. As can be seen above, both displacement/rotation and consistent force/moment vectors have been simplified by erasing the entries that are equal to zero due to the axisymmetric conditions.

The shell response may be decomposed in terms of normal modes, with a view to improve the computational performance of our model:

$$\mathbf{u}_{\mathrm{p},0}^\mathrm{s} = \boldsymbol{\Phi}_{\mathrm{p},0}^\mathrm{s} \mathbf{q}_0^\mathrm{s} \tag{7a}$$

$$\mathbf{u}_{\mathrm{p},0}^\mathrm{a} = \boldsymbol{\Phi}_{\mathrm{p},0}^\mathrm{a} \mathbf{q}_0^\mathrm{a} \tag{7b}$$

where $\boldsymbol{\Phi}_{\mathrm{p},0}^\mathrm{s}$, $\boldsymbol{\Phi}_{\mathrm{p},0}^\mathrm{a}$ are the modal matrices for the symmetric and anti-symmetric forms of $n = 0$, respectively, and $\mathbf{q}_0^\mathrm{s}$, $\mathbf{q}_0^\mathrm{a}$ denote the associated generalized coordinates. In particular, the modal matrices read:

$$\boldsymbol{\Phi}_{\mathrm{p},0}^\mathrm{s} = \begin{bmatrix} \mathbf{U}_0^\mathrm{s} \\ \mathbf{W}_0^\mathrm{s} \\ \mathbf{B}_0^\mathrm{s} \end{bmatrix}, \quad \boldsymbol{\Phi}_{\mathrm{p},0}^\mathrm{a} = \mathbf{V}_0^\mathrm{a} \tag{8}$$

where the modal sub-matrices $\mathbf{U}_0^\mathrm{s}$, $\mathbf{W}_0^\mathrm{s}$, $\mathbf{B}_0^\mathrm{s}$ and $\mathbf{V}_0^\mathrm{a}$ are defined as follows:

$$\mathbf{U}_0^\mathrm{s} = \begin{bmatrix} \mathbf{u}_{0,1}^\mathrm{s} & \mathbf{u}_{0,2}^\mathrm{s} & \cdots \end{bmatrix} \tag{9a}$$

$$\mathbf{W}_0^\mathrm{s} = \begin{bmatrix} \mathbf{w}_{0,1}^\mathrm{s} & \mathbf{w}_{0,2}^\mathrm{s} & \cdots \end{bmatrix} \tag{9b}$$

$$\mathbf{B}_0^\mathrm{s} = \begin{bmatrix} \boldsymbol{\beta}_{0,1}^\mathrm{s} & \boldsymbol{\beta}_{0,2}^\mathrm{s} & \cdots \end{bmatrix} \tag{9c}$$

$$\mathbf{V}_0^\mathrm{a} = \begin{bmatrix} \mathbf{v}_{0,1}^\mathrm{a} & \mathbf{v}_{0,2}^\mathrm{a} & \cdots \end{bmatrix} \tag{9d}$$

As can be seen in Eq. (8), the modal sub-matrices $\mathbf{V}_0^\mathrm{s}$, $\mathbf{U}_0^\mathrm{a}$, $\mathbf{W}_0^\mathrm{a}$ and $\mathbf{B}_0^\mathrm{a}$ are erased for convenience, since they are equal to zero. Therefore, the system of ordinary differential equations that governs the shell response is transformed to the space of generalized coordinates for the axial–radial motion (symmetric configuration) as follows:

$$\left( \boldsymbol{\Phi}_{\mathrm{p},0}^\mathrm{s} \right)^\mathrm{T} \mathbf{I}_{\mathrm{p},0}^\mathrm{s} \boldsymbol{\Phi}_{\mathrm{p},0}^\mathrm{s} \frac{\mathrm{d}^2 \mathbf{q}_0^\mathrm{s}}{\mathrm{d}t^2} + \left( \boldsymbol{\Phi}_{\mathrm{p},0}^\mathrm{s} \right)^\mathrm{T} \mathbf{L}_{\mathrm{p},0}^\mathrm{s} \boldsymbol{\Phi}_{\mathrm{p},0}^\mathrm{s} \mathbf{q}_0^\mathrm{s} = \left( \boldsymbol{\Phi}_{\mathrm{p},0}^\mathrm{s} \right)^\mathrm{T} \mathbf{p}_{\mathrm{p},0}^\mathrm{s} \tag{10}$$

and for the circumferential motion (anti-symmetric configuration) as:

$$\left( \boldsymbol{\Phi}_{\mathrm{p},0}^\mathrm{a} \right)^\mathrm{T} \mathbf{I}_{\mathrm{p},0}^\mathrm{a} \boldsymbol{\Phi}_{\mathrm{p},0}^\mathrm{a} \frac{\mathrm{d}^2 \mathbf{q}_0^\mathrm{a}}{\mathrm{d}t^2} + \left( \boldsymbol{\Phi}_{\mathrm{p},0}^\mathrm{a} \right)^\mathrm{T} \mathbf{L}_{\mathrm{p},0}^\mathrm{a} \boldsymbol{\Phi}_{\mathrm{p},0}^\mathrm{a} \mathbf{q}_0^\mathrm{a} = \left( \boldsymbol{\Phi}_{\mathrm{p},0}^\mathrm{a} \right)^\mathrm{T} \mathbf{p}_{\mathrm{p},0}^\mathrm{a} \tag{11}$$

Finally, the pile displacement/rotation vector $\mathbf{u}_\mathrm{p}$ and the line load vector $\mathbf{p}_\mathrm{p}$, based on the premise of axisymmetric response, may be written as:

$$\mathbf{u}_\mathrm{p} = \begin{bmatrix} \mathbf{u} \\ \mathbf{v} \\ \mathbf{w} \\ \boldsymbol{\beta}_z \end{bmatrix} = \begin{bmatrix} \mathbf{u}_0^\mathrm{s} \\ \mathbf{v}_0^\mathrm{a} \\ \mathbf{w}_0^\mathrm{s} \\ \boldsymbol{\beta}_{z,0}^\mathrm{s} \end{bmatrix}, \quad \mathbf{p}_\mathrm{p} = \begin{bmatrix} \mathbf{p}_{z,\mathrm{p}} \\ \mathbf{p}_{\theta,\mathrm{p}} \\ \mathbf{p}_{r,\mathrm{p}} \\ \mathbf{m}_{zz,\mathrm{p}} \end{bmatrix} = \frac{1}{2\pi R_\mathrm{p}} \begin{bmatrix} \mathbf{p}_{z0,\mathrm{p}}^\mathrm{s} \\ \mathbf{p}_{\theta 0,\mathrm{p}}^\mathrm{a} \\ \mathbf{p}_{r0,\mathrm{p}}^\mathrm{s} \\ \mathbf{m}_{zz0,\mathrm{p}}^\mathrm{s} \end{bmatrix} \tag{12}$$

### 3.2. Green's functions of a layered soil half-space via the thin-layer method

The present study considers the soil medium as a linear elastic layered half-space and its numerical treatment is accomplished using the Thin-Layer Method (TLM) (Kausel and Roësset, 1981). The TLM is

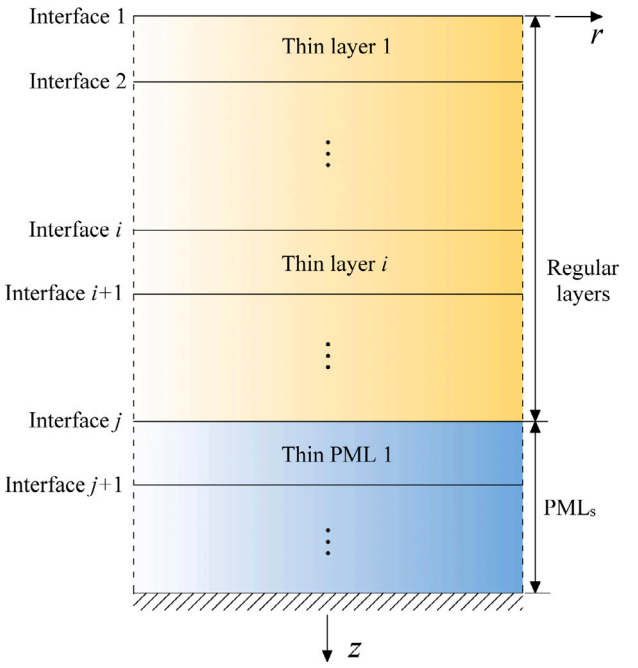


**Fig. 5.** A layered soil half-space modelled via the TLM+PMLs.

a semi-discrete technique based on the normal modes approach, which has been employed to obtain the dynamic response of layered media in a superbly efficient manner (Kausel, 1999). Briefly, a vertically inhomogeneous soil medium (comprised by homogeneous horizontal layers of dissimilar material properties) is discretized into thin horizontal layers in FE sense, i.e. the layer thickness is small compared to the excited wavelengths. To approximate the underlying half-space, Perfectly Matched Layers (PMLs) are utilized in this work (see Fig. 5). The key principle of PMLs lies in the complex-valued transformation of the spatial coordinates by means of complex stretching functions (Nguyen and Tassoulas, 2018; Kucukcoban et al., 2019). The coupling of PMLs with the TLM is not discussed in this paper for brevity, yet more details can be found in de Oliveira Barbosa et al. (2012) and Kausel and de Oliveira Barbosa (2012).

The application of both axial and torsional vibrations by the GDP shaker leads to excitation of all three motion components in both pile and soil. Therefore, the elicited wave motion in the soil medium includes both generalized Rayleigh (SV-P) and Love (SH) wave modes. Briefly, the generalized eigenvalue problem for the SV-P waves – in the context of the TLM – may be written as (Kausel and Roësset, 1981):

$$\left(k^2\bar{\mathbf{A}}+\bar{\mathbf{C}}\right)\begin{bmatrix}\boldsymbol{\phi}_r\\ k\boldsymbol{\phi}_z\end{bmatrix}=\begin{bmatrix}\mathbf{0}\\ \mathbf{0}\end{bmatrix} \tag{13}$$

and the generalized eigenvalue problem for the SH waves reads (Kausel and Roësset, 1981):

$$\left(k^2\mathbf{A}_\theta+\mathbf{C}_\theta\right)\boldsymbol{\phi}_\theta=\mathbf{0} \tag{14}$$

where $k$ is the radial wavenumber variable, and $\boldsymbol{\phi}_r$, $\boldsymbol{\phi}_\theta$, $\boldsymbol{\phi}_z$ denote the radial, circumferential and vertical modal displacements at the layer interfaces, respectively. Furthermore, the TLM matrices $\bar{\mathbf{A}}$, $\bar{\mathbf{C}}$, $\mathbf{C}_\theta$ are defined as:

$$\bar{\mathbf{A}}=\begin{bmatrix}\mathbf{A}_r & \mathbf{0}\\ \mathbf{B}_{zr} & \mathbf{A}_z\end{bmatrix} \tag{15}$$

$$\bar{\mathbf{C}}=\begin{bmatrix}\mathbf{G}_r-\omega^2\mathbf{M}_r & \mathbf{B}_{rz}\\ \mathbf{0} & \mathbf{G}_z-\omega^2\mathbf{M}_z\end{bmatrix} \tag{16}$$

$$\mathbf{C}_\theta=\mathbf{G}_\theta-\omega^2\mathbf{M}_\theta \tag{17}$$

It is noted that the TLM sub-matrices $\mathbf{A}_r$, $\mathbf{A}_\theta$, $\mathbf{A}_z$, $\mathbf{G}_r$, $\mathbf{G}_\theta$, $\mathbf{G}_z$, $\mathbf{M}_r$, $\mathbf{M}_\theta$ and $\mathbf{M}_z$ are associated with the soil domain as modelled by the coupled TLM+PMLs, i.e. including thin layers with complex-valued stretched thickness (de Oliveira Barbosa et al., 2012; Kausel and de Oliveira Barbosa, 2012); the sub-matrices $\mathbf{B}_{zr}$, $\mathbf{B}_{rz}$ remain unaffected by the complex-valued coordinate stretching.

We proceed to compute the Green's functions of a linear elastic layered half-space in the context of the TLM+PMLs. For that purpose, the explicit matrix expressions of the Green's functions in the frequency-(radial-azimuthal)-wavenumber domain are employed (Kausel, 1981; Kausel and Peek, 1982):

$$\hat{\mathbf{u}}_{\mathrm{s},n}=\begin{bmatrix}\hat{\mathbf{u}}_{r,n}\\ \hat{\mathbf{u}}_{\theta,n}\\ \hat{\mathbf{u}}_{z,n}\end{bmatrix}=\begin{bmatrix}\boldsymbol{\Phi}_r\mathbf{D}_\mathrm{R}\boldsymbol{\Phi}_r^\mathrm{T} & \mathbf{0} & k\boldsymbol{\Phi}_r\mathbf{K}_\mathrm{R}^{-1}\mathbf{D}_\mathrm{R}\boldsymbol{\Phi}_z^\mathrm{T}\\ \mathbf{0} & \boldsymbol{\Phi}_\theta\mathbf{D}_\mathrm{L}\boldsymbol{\Phi}_\theta^\mathrm{T} & \mathbf{0}\\ \frac{1}{k}\boldsymbol{\Phi}_z\mathbf{D}_\mathrm{R}\mathbf{K}_\mathrm{R}\boldsymbol{\Phi}_r^\mathrm{T} & \mathbf{0} & \boldsymbol{\Phi}_z\mathbf{D}_\mathrm{R}\boldsymbol{\Phi}_z^\mathrm{T}\end{bmatrix}\begin{bmatrix}\hat{\mathbf{p}}_{r,n}\\ \hat{\mathbf{p}}_{\theta,n}\\ \hat{\mathbf{p}}_{z,n}\end{bmatrix} \tag{18}$$

where $\hat{\mathbf{u}}_{r,n}$, $\hat{\mathbf{u}}_{\theta,n}$, $\hat{\mathbf{u}}_{z,n}$ are the vectors of soil displacements and $\hat{\mathbf{p}}_{r,n}$, $\hat{\mathbf{p}}_{\theta,n}$, $\hat{\mathbf{p}}_{z,n}$ are the vectors of applied loads, both expressed in the frequency-(radial-azimuthal)-wavenumber domain. The diagonal matrices $\mathbf{K}_\mathrm{R}$, $\mathbf{K}_\mathrm{L}$, $\mathbf{D}_\mathrm{R}$, $\mathbf{D}_\mathrm{L}$ are defined as:

$$\mathbf{K}_\mathrm{R}=\mathrm{diag}\left\{k_{\mathrm{R},1}\quad k_{\mathrm{R},2}\quad\cdots\right\} \tag{19}$$

$$\mathbf{K}_\mathrm{L}=\mathrm{diag}\left\{k_{\mathrm{L},1}\quad k_{\mathrm{L},2}\quad\cdots\right\} \tag{20}$$

$$\mathbf{D}_\mathrm{R}=\left(k^2\mathbf{I}-\mathbf{K}_\mathrm{R}^2\right)^{-1} \tag{21}$$

$$\mathbf{D}_\mathrm{L}=\left(k^2\mathbf{I}-\mathbf{K}_\mathrm{L}^2\right)^{-1} \tag{22}$$

where $k_{\mathrm{R},m}$ and $k_{\mathrm{L},m}$ denote the radial wavenumbers related to the generalized Rayleigh (SV-P) and generalized Love (SH) wave modes, respectively. Finally, the modal matrices $\boldsymbol{\Phi}_r$, $\boldsymbol{\Phi}_\theta$, $\boldsymbol{\Phi}_z$ are defined as:

$$\boldsymbol{\Phi}_r=\left[\boldsymbol{\phi}_{r,1}\quad\boldsymbol{\phi}_{r,2}\quad\cdots\right] \tag{23a}$$

$$\boldsymbol{\Phi}_\theta=\left[\boldsymbol{\phi}_{\theta,1}\quad\boldsymbol{\phi}_{\theta,2}\quad\cdots\right] \tag{23b}$$

$$\boldsymbol{\Phi}_z=\left[\boldsymbol{\phi}_{z,1}\quad\boldsymbol{\phi}_{z,2}\quad\cdots\right] \tag{23c}$$

For the problem at hand, the Green's functions are required due to: (i) unit radial ring sources at $r=R_\mathrm{p}$, (ii) unit circumferential ring sources at $r=R_\mathrm{p}$ and (iii) unit vertical ring sources at $r=R_\mathrm{p}$. Without further details, the vectors of soil displacements $\tilde{\mathbf{u}}_r$, $\tilde{\mathbf{u}}_\theta$, $\tilde{\mathbf{u}}_z$ may be readily expressed in terms of the associated rings loads $\tilde{\mathbf{p}}_{r,\mathrm{s}}$, $\tilde{\mathbf{p}}_{\theta,\mathrm{s}}$, $\tilde{\mathbf{p}}_{z,\mathrm{s}}$ in the frequency-space domain by virtue of the dynamic flexibility matrix $\tilde{\mathbf{F}}_\mathrm{s}$ as follows:

$$\tilde{\mathbf{u}}_\mathrm{s}=\begin{bmatrix}\tilde{\mathbf{u}}_{r,\mathrm{s}}\\ \tilde{\mathbf{u}}_{\theta,\mathrm{s}}\\ \tilde{\mathbf{u}}_{z,\mathrm{s}}\end{bmatrix}=\begin{bmatrix}\tilde{\mathbf{F}}_{rr} & \mathbf{0} & \tilde{\mathbf{F}}_{rz}\\ \mathbf{0} & \tilde{\mathbf{F}}_{\theta\theta} & \mathbf{0}\\ \tilde{\mathbf{F}}_{zr} & \mathbf{0} & \tilde{\mathbf{F}}_{zz}\end{bmatrix}\begin{bmatrix}\tilde{\mathbf{p}}_{r,\mathrm{s}}\\ \tilde{\mathbf{p}}_{\theta,\mathrm{s}}\\ \tilde{\mathbf{p}}_{z,\mathrm{s}}\end{bmatrix} \tag{24}$$

Due to the axisymmetric conditions of the problem, the vertical-radial and circumferential motions are uncoupled, leading to $\tilde{\mathbf{F}}_{r\theta}=\tilde{\mathbf{F}}_{\theta r}=\tilde{\mathbf{F}}_{z\theta}=\tilde{\mathbf{F}}_{\theta z}=\mathbf{0}$. It is noted that the load vectors $\tilde{\mathbf{p}}_{r,\mathrm{s}}$, $\tilde{\mathbf{p}}_{\theta,\mathrm{s}}$ and $\tilde{\mathbf{p}}_{z,\mathrm{s}}$ accommodate the pile–soil interaction loads and their formulation as external loads is owed to the solution method to be employed in the ensuing.

### 3.3. Pile–soil compatibility conditions during installation via the GDP method

The solution method to be followed herein has been developed and successfully applied in axial vibratory driving (Tsetas et al., 2023b). Specifically, the solution of this pile–soil problem is considered at discrete depths, at which the pile nodal rings and the soil layers interfaces (in the contact region) coincide. It is remarked that vector quantities corresponding to nodal rings and layer interfaces along the region of pile–soil contact are defined by the superscripts $(\cdot)^\mathrm{c}$. The compatibility conditions that hold in pile installation via the GDP method are identical with the ones valid for axial vibratory driving, with the addition of

the compatibility of circumferential tractions. Therefore, the following compatibility conditions are considered:
(i) continuity of radial displacements at the pile–soil interface:

$$\mathbf{w}^{\mathrm{c}} = \mathbf{u}^{\mathrm{c}}_{r}\Big|_{r=R_{\mathrm{p}}} \tag{25}$$

(ii) compatibility of vertical tractions applied at the pile–soil interface and the pile tip:

$$\mathbf{p}^{\mathrm{c}}_{z,\mathrm{s}} = -\mathbf{p}^{\mathrm{c}}_{z,\mathrm{p}}, \quad p^{(\mathrm{t})}_{z,\mathrm{s}} = -p^{(\mathrm{t})}_{z,\mathrm{p}} \tag{26}$$

in which the superscript (t) denotes the tip related component.
(iii) compatibility of radial tractions applied at the pile–soil interface:

$$\mathbf{p}^{\mathrm{c}}_{r,\mathrm{s}} = -\mathbf{p}^{\mathrm{c}}_{r,\mathrm{p}} \tag{27}$$

(iv) compatibility of circumferential tractions applied at the pile–soil interface:

$$\mathbf{p}^{\mathrm{c}}_{\theta,\mathrm{s}} = -\mathbf{p}^{\mathrm{c}}_{\theta,\mathrm{p}} \tag{28}$$

The soil reaction to driving is comprised by – following the axial vibratory driving model used as basis (Tsetas et al., 2023b) – a history-dependent frictional interface based on Coulomb friction and an elasto-plastic tip reaction formulation. The frictional interface formulation, due to the presence of circumferential motion, results into both vertical and circumferential friction forces. In particular, each pile material point slides (against the soil) along a 2-D cylindrical surface during GDP, instead of along a vertical line as in axial vibro-driving. Therefore, the friction force along the pile shaft is decomposed into:

$$p^{(i)}_{z,\mathrm{s}} = \frac{f^{(i)}_{\mathrm{s,ult}} l^{(i)} \dfrac{\partial u^{(i)}_{\mathrm{rel}}}{\partial t}}{\sqrt{\left(\dfrac{\partial u^{(i)}_{\mathrm{rel}}}{\partial t}\right)^2 + \left(\dfrac{\partial v^{(i)}_{\mathrm{rel}}}{\partial t}\right)^2}} \tanh\left(\frac{1}{v_{\mathrm{tol}}}\sqrt{\left(\frac{\partial u^{(i)}_{\mathrm{rel}}}{\partial t}\right)^2 + \left(\frac{\partial v^{(i)}_{\mathrm{rel}}}{\partial t}\right)^2}\right) \tag{29}$$

$$p^{(i)}_{\theta,\mathrm{s}} = \frac{f^{(i)}_{\mathrm{s,ult}} l^{(i)} \dfrac{\partial v^{(i)}_{\mathrm{rel}}}{\partial t}}{\sqrt{\left(\dfrac{\partial u^{(i)}_{\mathrm{rel}}}{\partial t}\right)^2 + \left(\dfrac{\partial v^{(i)}_{\mathrm{rel}}}{\partial t}\right)^2}} \tanh\left(\frac{1}{v_{\mathrm{tol}}}\sqrt{\left(\frac{\partial u^{(i)}_{\mathrm{rel}}}{\partial t}\right)^2 + \left(\frac{\partial v^{(i)}_{\mathrm{rel}}}{\partial t}\right)^2}\right) \tag{30}$$

where $v_{\mathrm{tol}}$ is a velocity tolerance parameter, $l^{(i)}$ is the length of influence derived from the FE projection and $f^{(i)}_{\mathrm{s,ult}}$ defines the amplitude of static (and kinetic) friction. It is noted that Eqs. (29) and (30) account for friction forces resulting from both the inner and outer pile surfaces; the distinction between the two contributions is beyond the scope of this model. Finally, the relative velocity is decomposed into a vertical and a circumferential component, i.e. $\frac{\partial u^{(i)}_{\mathrm{rel}}}{\partial t}$ and $\frac{\partial v^{(i)}_{\mathrm{rel}}}{\partial t}$, respectively, which are defined as follows:

$$\frac{\partial u^{(i)}_{\mathrm{rel}}}{\partial t} = \frac{\partial u^{(i)}}{\partial t} - \frac{\partial u^{(i)}_{z,\mathrm{s}}}{\partial t}\Big|_{r=R_{\mathrm{p}}} \tag{31}$$

$$\frac{\partial v^{(i)}_{\mathrm{rel}}}{\partial t} = \frac{\partial v^{(i)}}{\partial t} - \frac{\partial u^{(i)}_{\theta,\mathrm{s}}}{\partial t}\Big|_{r=R_{\mathrm{p}}} \tag{32}$$

The formulation of the friction interface is concluded with the hereditary law that governs the friction reduction mechanism – commonly termed as 'friction fatigue' (White and Lehane, 2004; Sheng et al., 2005; Moriyasu et al., 2018) – expressed as follows:

$$f^{(i)}_{\mathrm{s,ult}} = f^{(i)}_{\mathrm{s},0}\left(\beta_{\infty} + (1-\beta_{\infty})\mathrm{e}^{-c_N N^{(i)}_{\mathrm{cycl}}}\right) \tag{33}$$

where $\beta_{\infty}$ is the ratio of the ultimately degraded friction amplitude to the initial one ($f^{(i)}_{\mathrm{s},0}$), $c_N$ is a memory parameter that controls the rate of friction degradation and $N^{(i)}_{\mathrm{cycl}}$ is the number of loading cycles accumulated at the $i$–th soil interface during driving. In the case of GDP, it is postulated that loading cycles corresponding to vertical and circumferential friction forces contribute equally to the friction reduction, irrespectively of the dissimilar stress state induced in the surrounding soil and their frequency content; more details on these aspects are discussed in subsequent sections. In Fig. 6, a visualization of the friction force mechanism is given, where a 2-D bounding surface and the enclosed volume form the space of admissible values for the vertical ($p^{(i)}_{z,\mathrm{s}}$) and circumferential ($p^{(i)}_{\theta,\mathrm{s}}$) friction components. Furthermore, one of the two horizontal axes corresponds to the number of cycles $N_{\mathrm{cycl}}$, showcasing the reduction of the friction force norm $f^{(i)}_{\mathrm{s,ult}} l^{(i)}$ with the accumulation of loading cycles.

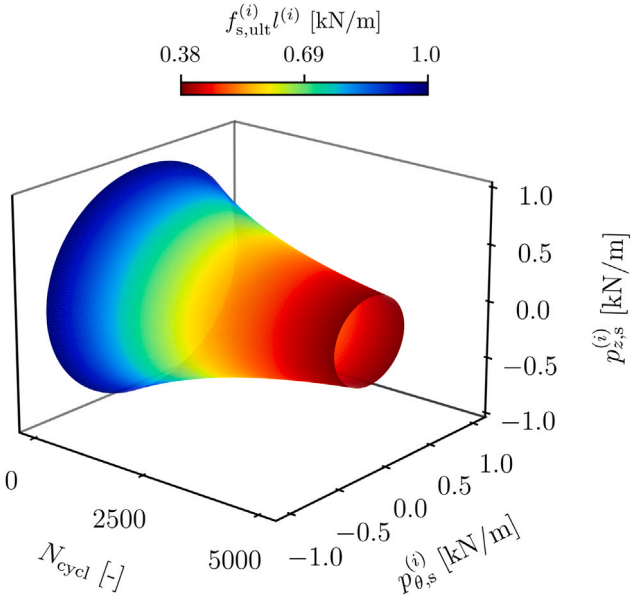


**Fig. 6.** History-dependent friction force at the $i$–th soil interface as a function of the number of loading cycles $N_{\mathrm{cycl}}$, for $f^{(i)}_{\mathrm{s},0} l^{(i)} = 1$ kN/m, $\beta_{\infty} = 0.2$, $c_N = 0.0003$.

Finally, an elastic-perfectly-plastic formulation is considered for the tip reaction as follows:

$$p^{(\mathrm{t})}_{z,\mathrm{s}} = -p^{(\mathrm{t})}_{z,\mathrm{p}} = \begin{cases} k_{\mathrm{t}}(u^{(\mathrm{t})}_{\mathrm{p}} - u_{\mathrm{pl}}), & |k_{\mathrm{t}}(u^{(\mathrm{t})}_{\mathrm{p}} - u_{\mathrm{pl}})| < f_{\mathrm{t,ult}} h_{\mathrm{p}} \\ f_{\mathrm{t,ult}} h_{\mathrm{p}} \mathrm{sgn}\left(\dfrac{\partial u^{(\mathrm{t})}_{\mathrm{p}}}{\partial t}\right), & |k_{\mathrm{t}}(u^{(\mathrm{t})}_{\mathrm{p}} - u_{\mathrm{pl}})| = f_{\mathrm{t,ult}} h_{\mathrm{p}} \end{cases} \tag{34}$$

where $u_{\mathrm{pl}}$ is the plastic tip displacement, $f_{\mathrm{t,ult}}$ is the plastic tip resistance and $k_{\mathrm{t}}$ is the stiffness coefficient. The latter is extracted from the last diagonal entry of the soil dynamic stiffness matrix $\widetilde{\mathbf{K}}_{\mathrm{s}}$ (corresponding to the pile tip); the matrix $\widetilde{\mathbf{K}}_{\mathrm{s}}$ is obtained via inversion of the dynamic flexibility matrix $\widetilde{\mathbf{F}}_{\mathrm{s}}$ via spectral decomposition. As can be seen, the tip reaction is based solely on the axial response of the pile tip without any effects due to the circumferential motion. This choice will be elaborated further in the discussion of the numerical results and the field data.

## 4. A time–frequency solution method based on the adjusted harmonic balance method

In the ensuing, a hybrid time–frequency method is pursued, based on the Alternating Frequency–Time (AFT) Harmonic Balance Method (HBM) (Krack and Gross, 2019; Cameron and Griffin, 1989). This method has been widely adopted in the study of mechanical systems under harmonic/periodic excitation, e.g. non-linear energy harvesters (Zhou et al., 2016), buckling analysis of composite plates

(Juhász and Szekrényes, 2015) and reduced-order modelling of bladed discs in turbomachinery (Quaegebeur et al., 2022). The proposed approach employs the HBM as the basis for a sequential scheme in which the pile–soil response is postulated to be virtually periodic "microscopically", i.e. for a small time interval around a certain state of the system. Subsequently, assemblage of these solutions via linear interpolation of the response Fourier coefficients in time leads to a quasi-periodic response due to slow amplitude modulation of the involved harmonic components. The preceding approach was validated numerically and was successfully applied to vibratory pile installation (Tsetas et al., 2023b, 2022).

During pile installation via the GDP method, a low-frequency ($\Omega_\mathrm{a}$) axial and a high-frequency ($\Omega_\mathrm{t}$) torsional excitation are applied simultaneously at the pile top. Most likely the torsional driving frequency will not be an integer multiple of the axial one, due to the impracticality of imposing a truly integer ratio $\Omega_\mathrm{t}/\Omega_\mathrm{a}$ or even by choice, e.g. to avoid potential interaction that may lead to shaker damage. Hence, the premise of periodic pile–soil response (for a single state) with the axial driving frequency as the fundamental one is invalidated. Therefore, a modification of the classical HBM is required to render our framework applicable in the case of GDP method.

An efficient alternative for quasi-periodic problems has been proposed by Guskov and Thouverez (2012), based on a mono-harmonic approximation of multiple fundamental frequencies leading to the so-called adjusted HBM (AHBM). The latter method is identical to the classical HBM, albeit based on a new fundamental frequency $\Omega_0$ that is the greatest common divisor of $\bar{\Omega}_\mathrm{t}$ and $\bar{\Omega}_\mathrm{a}$:

$$\Omega_0 = \frac{\bar{\Omega}_\mathrm{t}}{\kappa_\mathrm{t}} = \frac{\bar{\Omega}_\mathrm{a}}{\kappa_\mathrm{a}} \tag{35}$$

where $\kappa_\mathrm{a}$, $\kappa_\mathrm{t}$ are appropriate integers to approximate the original frequency ratio $\eta_\Omega = \Omega_\mathrm{t}/\Omega_\mathrm{a}$ up to the desired precision and the approximate frequencies $\bar{\Omega}_\mathrm{t}$, $\bar{\Omega}_\mathrm{a}$ are obtained as follows:

$$\eta_\Omega = \frac{\Omega_\mathrm{t}}{\Omega_\mathrm{a}} \approx \bar{\eta}_\Omega = \frac{\bar{\Omega}_\mathrm{t}}{\bar{\Omega}_\mathrm{a}} = \frac{\kappa_\mathrm{t}}{\kappa_\mathrm{a}} \tag{36}$$

where the rational number $\bar{\eta}_\Omega$ is the new approximate frequency ratio. Accordingly, a generic response quantity $f(t)$ may be assumed to possess the following form in the context of the AHBM:

$$f(t) = \sum_{j\in S_0} \left(c_j \cos(j\Omega_0 t) + s_j \sin(j\Omega_0 t)\right) \tag{37}$$

where the set $S_0$ is defined as follows:

$$S_0 = \left\{ i_1\kappa_\mathrm{a} + i_2\kappa_\mathrm{t} \;\middle|\; i_1 \in \left[-h_\mathrm{a}, h_\mathrm{a}\right],\ i_2 \in \left[-h_\mathrm{t}, h_\mathrm{t}\right] \right\} \tag{38}$$

where $i_1$, $i_2$ can obtain integer values from the designated intervals and $h_\mathrm{a}$, $h_\mathrm{t}$ are positive integers that denote the truncation limits of the super-harmonics to be included.

The targeted harmonics in the AHBM encompass the two distinct sets of super-harmonic components associated with the two fundamental frequencies, as well as the harmonics that may emerge from the interaction of the previous two sets. It is noted that certain values of $j$ may be generated by more than one pair of ($i_1$, $i_2$), so only one term is retained in these scant cases, and the number of terms can be further reduced by virtue of the symmetries of the Fourier series. For the present problem, approximation of $\eta_\Omega$ up to the second decimal place is considered.

Accordingly, the assumed solutions for the case of the GDP method possess a new base frequency, i.e. $\Omega_0$ as defined above. Without further delay, the pile generalized coordinates are defined as follows:

$$q^\mathrm{s}_{0,m} = \begin{cases} c^\mathrm{s}_{0,0} t + \sum\limits_{j\in S_0} \left(c^\mathrm{s}_{0,j} \cos(j\Omega_0 t) + s^\mathrm{s}_{0,j} \sin(j\Omega_0 t)\right), & m = 0 \\ c^\mathrm{s}_{m,0} + \sum\limits_{j\in S_0} \left(c^\mathrm{s}_{m,j} \cos(j\Omega_0 t) + s^\mathrm{s}_{m,j} \sin(j\Omega_0 t)\right), & m > 0 \end{cases} \tag{39}$$

$$q^\mathrm{a}_{0,m} = c^\mathrm{a}_{m,0} + \sum_{j\in S_0} \left(c^\mathrm{a}_{m,j} \cos(j\Omega_0 t) + s^\mathrm{a}_{m,j} \sin(j\Omega_0 t)\right), \quad m \geq 0 \tag{40}$$

where $\mathbf{c}^\mathrm{s}_m = \begin{bmatrix} c^\mathrm{s}_{m,0} & c^\mathrm{s}_{m,1} & \cdots \end{bmatrix}^\mathrm{T}$ and $\mathbf{s}^\mathrm{s}_m = \begin{bmatrix} s^\mathrm{s}_{m,1} & s^\mathrm{s}_{m,2} & \cdots \end{bmatrix}^\mathrm{T}$ denote the vectors of Fourier coefficients associated with the $m$–th axial–radial mode; similarly, the Fourier coefficients of the $m$–th torsional mode are arranged in the vectors $\mathbf{c}^\mathrm{a}_m = \begin{bmatrix} c^\mathrm{a}_{m,0} & c^\mathrm{a}_{m,1} & \cdots \end{bmatrix}^\mathrm{T}$ and $\mathbf{s}^\mathrm{a}_m = \begin{bmatrix} s^\mathrm{a}_{m,1} & s^\mathrm{a}_{m,2} & \cdots \end{bmatrix}^\mathrm{T}$. Furthermore, the vertical and circumferential friction forces along the pile–soil interface may be expressed as:

$$\mathbf{p}^\mathrm{c}_{\mathrm{s},z} = \boldsymbol{\Psi}_z \left( \boldsymbol{\alpha}_{z0} + \sum_{j\in S_0} \left(\boldsymbol{\alpha}_{zj} \cos(j\Omega_0 t) + \boldsymbol{\beta}_{zj} \sin(j\Omega_0 t)\right) \right) \tag{41}$$

$$\mathbf{p}^\mathrm{c}_{\mathrm{s},\theta} = \boldsymbol{\Psi}_\theta \left( \boldsymbol{\alpha}_{\theta 0} + \sum_{j\in S_0} \left(\boldsymbol{\alpha}_{\theta j} \cos(j\Omega_0 t) + \boldsymbol{\beta}_{\theta j} \sin(j\Omega_0 t)\right) \right) \tag{42}$$

in which $\boldsymbol{\alpha}_{zj} = \begin{bmatrix} \alpha_{zj,0} & \alpha_{zj,1} & \cdots \end{bmatrix}^\mathrm{T}$, $\boldsymbol{\beta}_{zj} = \begin{bmatrix} \beta_{zj,1} & \beta_{zj,2} & \cdots \end{bmatrix}^\mathrm{T}$ are the vectors of Fourier coefficients related to the $j$–th cosine and sine terms, respectively, and $\boldsymbol{\Psi}_z$ is the matrix encapsulating the basis vectors for the vertical friction forces. Correspondingly, the vectors of Fourier coefficients for the circumferential friction forces are denoted as $\boldsymbol{\alpha}_{\theta j} = \begin{bmatrix} \alpha_{\theta j,0} & \alpha_{\theta j,1} & \cdots \end{bmatrix}^\mathrm{T}$, $\boldsymbol{\beta}_{\theta j} = \begin{bmatrix} \beta_{\theta j,1} & \beta_{\theta j,2} & \cdots \end{bmatrix}^\mathrm{T}$ and $\boldsymbol{\Psi}_\theta$ is the matrix containing the basis vectors for spatial approximation of the circumferential friction forces. Finally, the axial tip reaction is also assumed to be periodic:

$$p^{(\mathrm{t})}_{\mathrm{s},z} = \alpha_{\mathrm{t},0} + \sum_{j\in S_0} \left(\alpha_{\mathrm{t},j} \cos(j\Omega_0 t) + \beta_{\mathrm{t},j} \sin(j\Omega_0 t)\right) \tag{43}$$

where $\boldsymbol{\alpha}_\mathrm{t} = \begin{bmatrix} \alpha_{\mathrm{t},0} & \alpha_{\mathrm{t},1} & \cdots \end{bmatrix}^\mathrm{T}$ and $\boldsymbol{\beta}_\mathrm{t} = \begin{bmatrix} \beta_{\mathrm{t},1} & \beta_{\mathrm{t},2} & \cdots \end{bmatrix}^\mathrm{T}$ denote the vectors encapsulating the Fourier coefficients of the tip reaction.

By substituting the assumed solutions into the dynamic equilibria of pile and soil and the compatibility conditions, the following residuals are obtained:

$$\mathbf{r}_{\mathrm{c},z} = \boldsymbol{\Psi}^\mathrm{T}_z \left( \mathbf{p}^\mathrm{c}_{z,\mathrm{s}} + \mathbf{p}^\mathrm{c}_{z,\mathrm{p}} \right) \tag{44a}$$

$$\mathbf{r}_{\mathrm{c},\theta} = \boldsymbol{\Psi}^\mathrm{T}_\theta \left( \mathbf{p}^\mathrm{c}_{\theta,\mathrm{s}} + \mathbf{p}^\mathrm{c}_{\theta,\mathrm{p}} \right) \tag{44b}$$

$$r_\mathrm{t} = p^{(\mathrm{t})}_{z,\mathrm{s}} + p^{(\mathrm{t})}_{z,\mathrm{p}} \tag{44c}$$

$$\mathbf{r}_{q,\mathrm{s}} = \left(\boldsymbol{\Phi}^\mathrm{s}_{\mathrm{p},0}\right)^\mathrm{T} \left( \mathbf{I}^\mathrm{s}_{\mathrm{p},0} \boldsymbol{\Phi}^\mathrm{s}_{\mathrm{p},0} \frac{\mathrm{d}^2 \mathbf{q}^\mathrm{s}_0}{\mathrm{d}t^2} + \mathbf{L}^\mathrm{s}_{\mathrm{p},0} \boldsymbol{\Phi}^\mathrm{s}_{\mathrm{p},0} \mathbf{q}^\mathrm{s}_0 - \mathbf{p}^\mathrm{s}_{\mathrm{p},0} \right) \tag{44d}$$

$$\mathbf{r}_{q,\mathrm{a}} = \left(\boldsymbol{\Phi}^\mathrm{a}_{\mathrm{p},0}\right)^\mathrm{T} \left( \mathbf{I}^\mathrm{a}_{\mathrm{p},0} \boldsymbol{\Phi}^\mathrm{a}_{\mathrm{p},0} \frac{\mathrm{d}^2 \mathbf{q}^\mathrm{a}_0}{\mathrm{d}t^2} + \mathbf{L}^\mathrm{a}_{\mathrm{p},0} \boldsymbol{\Phi}^\mathrm{a}_{\mathrm{p},0} \mathbf{q}^\mathrm{a}_0 - \mathbf{p}^\mathrm{a}_{\mathrm{p},0} \right) \tag{44e}$$

which can be arranged in the following residual vector:

$$\mathbf{r} = \begin{bmatrix} \mathbf{r}_{\mathrm{c},z} \\ \mathbf{r}_{\mathrm{c},\theta} \\ r_\mathrm{t} \\ \mathbf{r}_{q,\mathrm{s}} \\ \mathbf{r}_{q,\mathrm{a}} \end{bmatrix} \tag{45}$$

Based on the AHBM, the Fourier coefficients of the residual vector $\mathbf{r}$ are obtained via a Fourier–Galerkin projection and are required to vanish:

$$\mathbf{R}_\mathrm{F} = \frac{1}{T_0} \int_0^{T_0} \mathbf{r}\mathbf{h}\, \mathrm{d}t \tag{46}$$

where $\mathbf{R}_\mathrm{F}$ is the Fourier coefficients matrix of the residuals, $T_0$ is the period corresponding to the base frequency of the AHBM ($\Omega_0$) and the row vector $\mathbf{h}$ encapsulates the test functions (i.e. Fourier harmonics) $h_i(t)$ defined as:

$$h_i(t) = \frac{1}{2} \left[ \left(1 + (-1)^i\right) \cos\left(\frac{i\Omega_0 t}{2}\right) + \left(1 + (-1)^{i+1}\right) \sin\left(\frac{i+1}{2}\Omega_0 t\right) \right] \tag{47}$$

Based on the previous, the AHBM is used as basis in our sequential scheme, enabling to capture harmonic components associated with both axial and torsional driving frequencies.

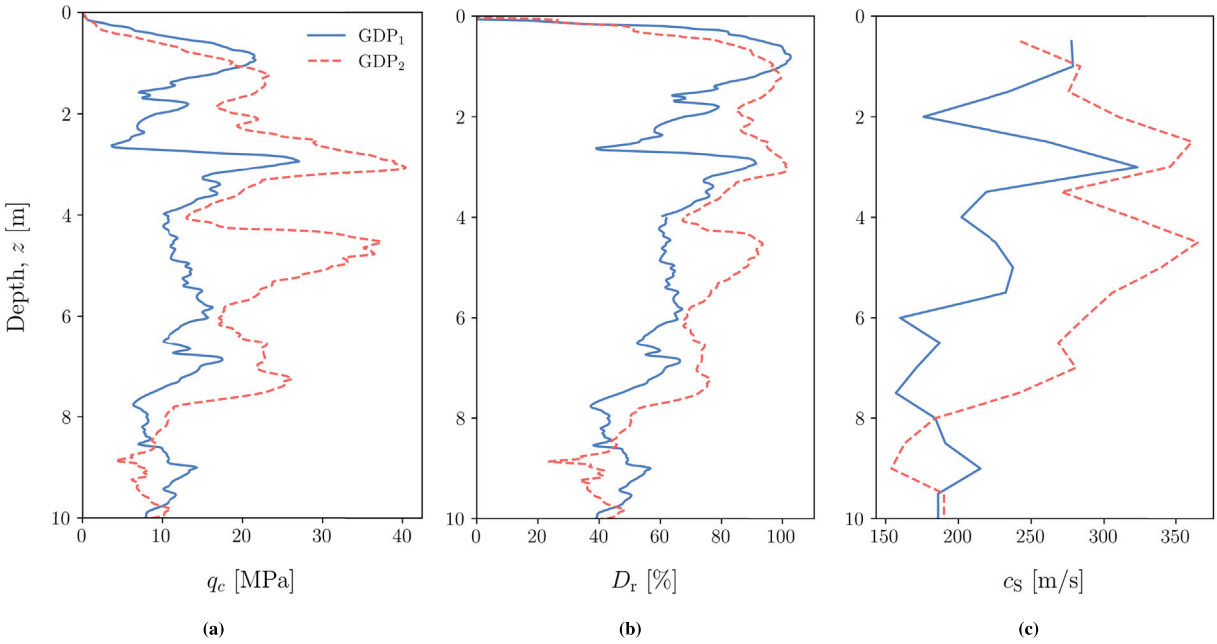


**Fig. 7.** Profiles of (a) cone tip resistance ($q_c$), (b) relative density ($D_r$), and (c) shear wave velocity ($c_S$) obtained from the SCPTu's.

**Table 2**
Properties of the piles driven in the GDP field campaign.

| $\rho_p$ [kg/m$^3$] | $E_p$ [Pa] | $\nu_p$ [–] | $L_p$ [m] | $R_p$ [m] | $h_p$ [m] |
|---|---|---|---|---|---|
| 7850 | $210 \cdot 10^9$ | 0.3 | 10 | 0.373 | 0.0159 |

**Table 3**
Driving frequencies for the GDP installation tests.

| | | $GDP_1$ | $GDP_2$ |
|---|---|---|---|
| Axial driving frequency | $f_a$ [Hz] | 16.3 | 16.5 |
| Torsional driving frequency | $f_t$ [Hz] | 62.6 | 63.0 |

## 5. Numerical results and comparison with field data

The preceding conclude the numerical developments of this paper, by presenting a computational framework applicable for the analysis of pile driving via axial vibratory and GDP techniques; further details about their derivation and validation can be found in Tsetas (2023). In the ensuing, the characterization of the GDP model parameters is presented on the basis of *in-situ* tests from the GDP field campaign (Tsetas et al., 2023a). Numerical results are compared against field data showcasing the model potential and further investigation into the GDP method uncovers the mechanisms that lead to its remarkable installation performance. Finally, the soil response during pile driving by GDP is studied, with a view to investigate the characteristics of the induced wave motion.

### 5.1. Model predictions and installation measurements

The installation process is studied for an embedment interval from 3 m to 8 m, with the aid of field data from two piles driven via the GDP method (i.e. $GDP_1$ and $GDP_2$). The dynamic input excitation – both axial and circumferential – is inferred from strain measurements at the pile top, which were monitored by means of fibre Bragg grating (FBG) sensors. Furthermore, the properties of the GDP piles driven in the field campaign can be found in Table 2 and the installation settings for both tests are given in Table 3. As regards the characterization of the soil medium, Seismic Cone Penetration Tests with pore water pressure measurements (SCPTu's) were performed and the depth of the water table was found at 4.5 m (see Fig. 7). It is noted that material dissipation is introduced in the form of frequency-independent hysteretic damping for both pile and soil with ratios $\xi_p = 0.001$ and $\xi_s = 0.025$ (identical for P- and S-waves), respectively.

The present modelling framework is aimed to be applicable for the analysis of both axial vibratory and GDP methods. The motivation to retain the formulation of the two models as common as possible lies in the similarity of the installation process (in terms of physics) between the two methods; to put it simply a physically sound model for GDP should be capable to capture axial vibratory driving as well. With a view to proposing a unified modelling framework, the frictional interface and tip reaction formulations of the axial vibratory model are employed and adjusted to a minimal degree to accommodate the additional requirements for the GDP method.

As regards the frictional interface, the generic dependence of friction force on relative velocity directly encompasses the case of GDP; however, the question about the parameter calibration for the memory mechanism may be raised. We proceed to retain the expression $f_{s,0}^{(i)} = 0.012 q_c(z_i)$ and the value $\beta_\infty = 0.2$, as used for the vibro-driven pile in the GDP campaign (Tsetas et al., 2023a). Subsequently, for the degradation rate parameter $c_N$ an admissible range of values (i.e. $c_N = 0.0003 - 0.0005$) is considered, as proposed in Tsetas et al. (2023b). Furthermore, the tip reaction brings about the complication of the additional circumferential component and its coupling with the axial one. Due to the lack of a dataset that may facilitate the distinction of such effects, the following choices are made: (i) the torsional reaction at the tip is discarded and (ii) the effect of torsion is accounted by modifying the axial tip reaction. Effectively, this approach retains the parameter $k_t$ as defined in the axial vibratory model (Tsetas et al., 2023b), whereas the value of the plastic tip resistance $f_{t,ult}$ is modified. These considerations allow to circumvent the introduction of additional parameters, which would be inescapable if axial-torsional reaction coupling and/or torsional reaction were to be considered.

In Fig. 8, the GDP model predictions are compared with the pile penetration ($u_R$) records from the GDP field campaign. To achieve a first proper validation of the drivability model, the calibrated parameters for $GDP_1$ and $GDP_2$ were aimed to be identical. This validation process was successful and resulted in: (i) adoption of $c_N = 0.0003$ for

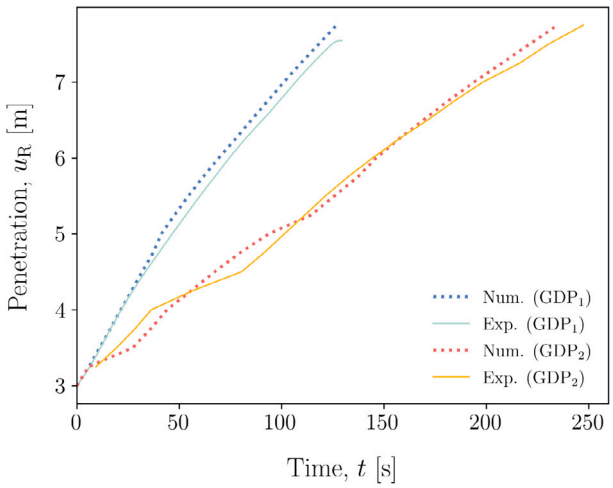


**Fig. 8.** Comparison of pile penetration ($u_R$) between numerical model predictions and experimental data for the piles GDP$_1$ and GDP$_2$.

the shaft reaction and (ii) setting $f_{t,ult} = 0.15q_c$ for the tip reaction. The value of the degradation parameter falls in the range proposed for the axial vibro-driving model (Tsetas et al., 2023b), whereas the modification of tip reaction is considered as a result of the axial-torsional coupling at the pile tip. The latter modification is an efficient manner to address a presumably more complicated mechanism, which is yet to be fully comprehended and can be better identified by means of additional experiments. As can be seen in Fig. 8, these two calibration options lead to great agreement between the numerical predictions and the penetration records for both GDP$_1$ and GDP$_2$. Naturally, further refinement of the calibration process is of utmost importance for future development; yet the degree of agreement with field data achieved through a single calibration and for two different piles is more than promising.

### 5.2. Redirection of the friction force vector: the major driving mechanism of GDP

The previous showcased the predictive potential of the present numerical model. However, the mechanics of the process are yet to be deciphered, with a view to comprehend the driving mechanism of GDP. As postulated in Section 2, the introduction of torsion will mobilize friction in the circumferential direction, thus the vertical soil reaction along the shaft will be reduced. This hypothesis is confirmed by the friction forces developed at the pile shaft, based on the numerical results of the present model. Specifically, the vertical and circumferential (line) friction forces at elevation of $z = 3$ m below the ground surface are displayed in Fig. 9; the chosen time window corresponds to penetration depth of 5.5 m. As can be seen, both friction force components have a common pattern, irrespectively of the pile location (GDP$_1$ or GDP$_2$). It is noted that the friction forces at different elevations and for different penetration depth possess the same pattern observed in Fig. 9, thereby such results are not presented to avoid content repetition. As can be seen, the friction force is predominantly expended in the circumferential direction resisting the torsional motion and is accompanied by a substantially lower friction force along the vertical direction. It is concluded that the redirection of the friction force vector emerges as the primary driving mechanism of GDP, by virtue of major reduction of the soil reaction along the penetration axis.

Another visualization of the friction force vector during the studied time interval is presented in Fig. 10. Specifically, the trajectory of the friction force vector is shown for the cases discussed in Fig. 9. Two loci may be distinguished, namely two horizontal lines, and the majority of the friction force points are seen to clusters around them. In particular, these two lines (loci) correspond to the cases of zero vertical friction and the extrema of circumferential friction force. This is an additional testament to the mechanism of friction redirection, as the friction force approaches the extrema in the circumferential direction and the extrema of vertical friction are scarcely present. It is noted that a fixed time step of $\Delta t = 0.0001$ s has been used for the evaluation of the friction force vectors in the previous plots.

In Figs. 9 and 10, it appears that the friction norm does not alter, as it would be expected due to friction fatigue. The time window of the preceding plots has a duration of 0.2 s, facilitating the observation of the friction forces at a time scale governed by the driving frequency. However, the friction force reduction according to the proposed memory mechanism evolves at a much slower time scale, thus the respective effects require more than 100 cycles to be apparent. For that purpose, the evolution of the friction force norm during installation is shown in Figs. 11(a) and 11(b) for GDP$_1$ and GDP$_2$, respectively. It is remarked that the dotted horizontal plateaus correspond to time intervals where the pile has not reached the respective soil depth and therefore the friction force is not present yet (i.e. no pile–soil contact).

Following the preceding investigations, the ratio of circumferential to total friction force is an interesting metric to obtain further insight into the mechanics of GDP. In Fig. 12, the aforementioned ratio is mapped along the soil depth (in contact with the pile) and during the installation time windows described above. It can be observed that the friction ratio appears to slightly decrease overall with penetration depth; the region with the lowest friction ratio is consistently found to be close to the pile tip. This outcome is rational (based on the CPT profile), as the soil reaction closer to the tip is the least degraded due to the small number of accumulated loading cycles (i.e. friction fatigue).

Another interesting aspect of GDP is the power redistribution that follows from the introduction of torsion. Specifically, the quantity of interest is the dissipated power along the pile–soil interface and at the pile tip. It is apparent that in the case of axial vibratory driving, power is dissipated solely due to the friction along the vertical axis and the tip reaction. In Fig. 13, a comparison in terms of dissipated power is presented due to: (i) the vertical friction forces, (ii) the circumferential friction forces and (iii) the vertical tip reaction. Evidently, the preponderance of dissipated power corresponds to circumferential friction, whereas vertical friction forces and tip reaction have approximately similar contribution (yet marginal overall). The latter finding implies that in GDP – upon successfully diverting shaft reaction in the circumferential direction – the vertical shaft and tip reactions are comparable, thus differentiating from the classical vibro-driving, where the vertical shaft reaction (also total shaft reaction) is the major component. Conclusively, the friction redirection mechanism irrefutably benefits the installation process in terms of performance, yet it implies that the driving-induced soil motion is dissimilar from axial vibratory driving. Section 5.3 is focused on this aspect, namely the investigation of the soil response characteristics in the case of GDP.

### 5.3. Characteristics of the induced ground motion due to pile installation via GDP

From the preceding findings, it is deduced that the friction redirection mechanism may imply a dissimilar disturbance in the soil medium compared to standard vibratory driving. To further investigate this aspect, the soil response during the installation of pile GDP$_1$ is studied. For that purpose, in Fig. 14 the peak particle velocities (PPVs) throughout the soil domain are shown for both SV-P and SH wavefields, in the form of contour fields in the $r - z$ plane and at $u_R = 5.5$ m. It is noted that the displayed patterns do not resemble the wavefield at any instant, as they are not snapshots of the response; these graphs present a collection of the PPVs for all soil material points attained during the studied time window (sufficient for stationary response). As can be seen, the first major observation consists in the significantly lower PPVs associated with the SV-P wavefield compared to the SH

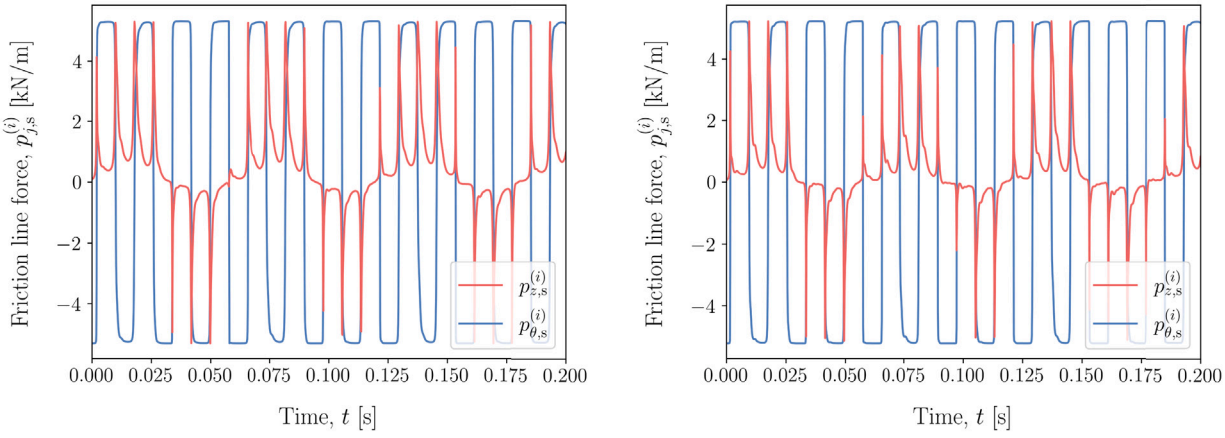


**(a)** $GDP_1$ **(b)** $GDP_2$

**Fig. 9.** Friction force components ($p_{z,s}^{(i)}$, $p_{\theta,s}^{(i)}$) at $z_i = 3.0$ m and $u_R = 5.5$ m.

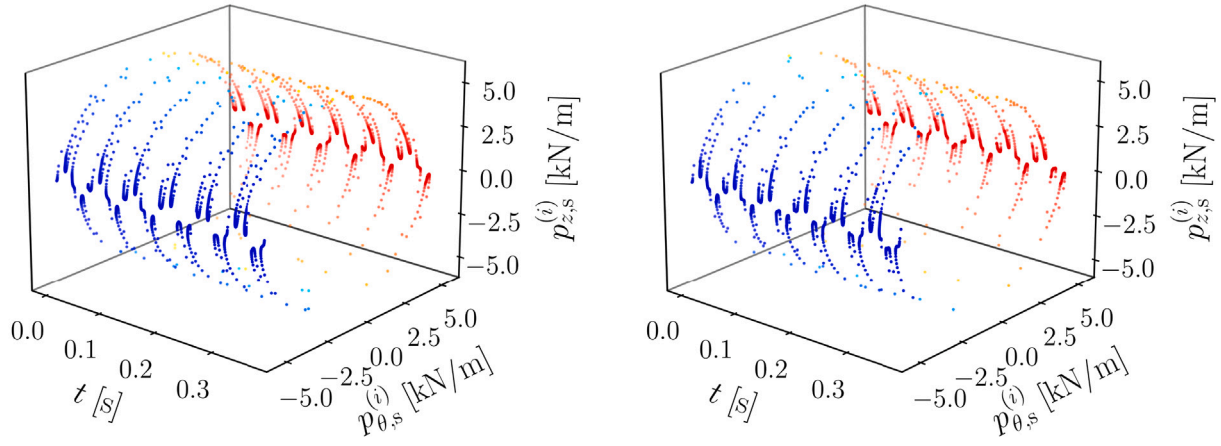


**(a)** $GDP_1$ **(b)** $GDP_2$

**Fig. 10.** Friction force trajectories at $z_i = 3.0$ m and $u_R = 5.5$ m; the colour of the markers is based on the ratio of circumferential to total friction force, i.e. ranging from −1 (blue) to 1 (red).

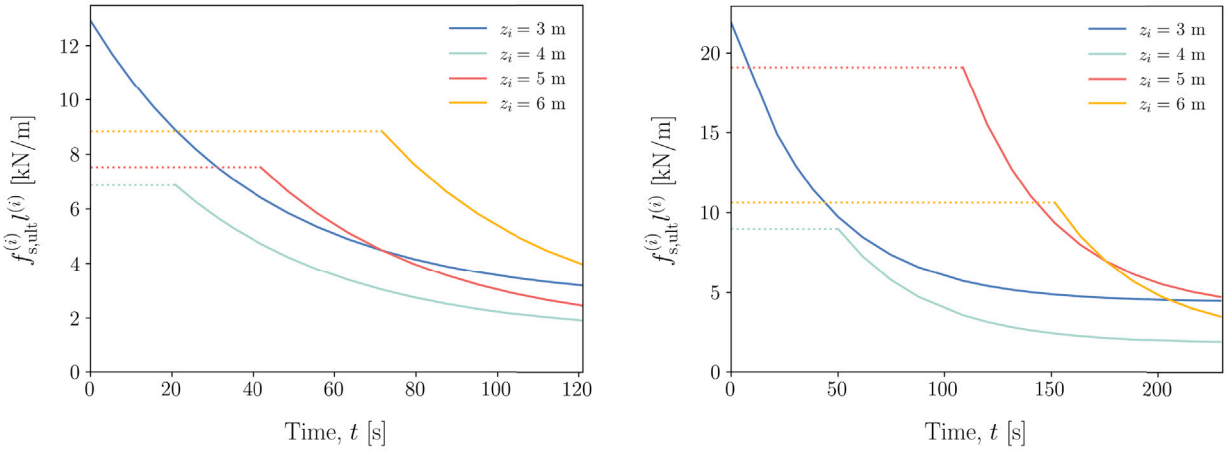


**(a)** $GDP_1$ **(b)** $GDP_2$

**Fig. 11.** Friction force norm ($f_{s,ult}^{(i)} l^{(i)}$) of the soil interfaces $z_i = 3.0$ m, $z_i = 4.0$ m, $z_i = 5.0$ m and $z_i = 6.0$ m during the installation process.

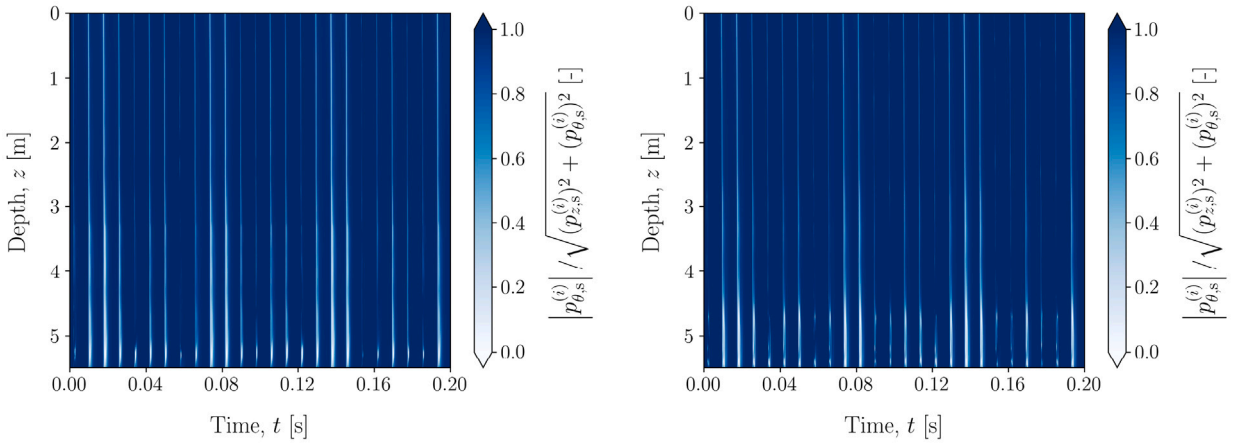


**(a)** $GDP_1$ **(b)** $GDP_2$

**Fig. 12.** Ratio of circumferential to total friction force $\left|p_{\theta,s}^{(i)}\right| / \sqrt{(p_{z,s}^{(i)})^2 + (p_{\theta,s}^{(i)})^2}$ at $u_R = 5.5$ m.

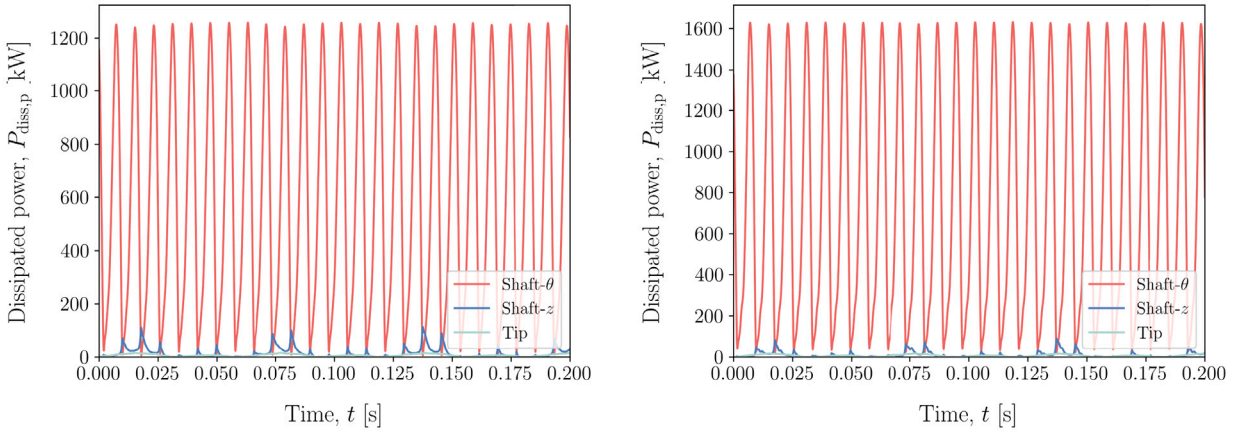


**(a)** $GDP_1$ **(b)** $GDP_2$

**Fig. 13.** Comparison of power dissipated by (i) circumferential shaft reaction, (ii) vertical shaft reaction and (iii) tip reaction at $u_R = 5.5$ m.

wavefield. This observation is consistent with the main hypothesis of GDP and the previous results, as the high-frequency torsion mobilizes the preponderance of friction forces in the circumferential direction and thus elicits SH waves. As a result the intensity of the SV-P motion may drop substantially compared to axial vibratory driving. The significance of the previous finding cannot be overemphasized; potential abatement of the SV-P wavefield and thus of Rayleigh waves is directly related to greatly reducing the environmental disturbance of onshore pile driving activities. As regards the offshore environment, pile driving elicits interface waves emanating from the SV-P wavefield at the seabed surface (Tsouvalas and Metrikine, 2016), namely the Scholte waves (Jensen et al., 2011; Aki and Richards, 2002). Therefore, the potential abatement of the SV-P wavefield can positively affect the associated underwater noise emissions during pile installation via GDP. These findings are in line with the envisaged goals of GDP, namely the reduction of the induced disturbance in the surrounding medium – accompanied by enhancement of installation performance – compared to axial vibratory driving.

To further complement the preceding discussion, we conclude the study of the driving-induced soil motion with particle trajectories at the ground surface. In Fig. 15, the trajectories of soil particles for multiple receiver radii are depicted for pile $GDP_1$. In the case of axial vibratory driving, the surface motion is predominantly vertical for small receiver radii, whereas with increasing distance from the source the trajectories transition from vertically-polarized orbits to retrograde elliptical orbits (typical of Rayleigh waves) (Masoumi et al., 2007, 2009). These orbit patterns are also observed for GDP, with the discrepancy that the frequency content is much richer – due to the associated vertical friction forces (see Fig. 9) – as testified by the respective orbits in Fig. 15(a). Naturally, these components decay quickly with radius and at larger receiver distances the characteristic trajectories of Rayleigh waves – related to lower frequencies – are dominant. This remark is also corroborated by Figs. 15(b) and 15(c) where both $u_{r,s}^{(0)}$ and $u_{z,s}^{(0)}$ (SV-P) components appear to surpass the magnitude of the circumferential (SH) component $u_{\theta,s}^{(0)}$ at large receiver radius. Conclusively, the soil motion results showcase that the energy introduced into the soil medium is expressed primarily in SH wave motion and the elicited SV-P wavefield possesses appreciably lower amplitude, yet in large distances the SV-P motion dominates in the form of Rayleigh waves.

The preceding findings cannot be generalized a priori for any scenario of GDP. In particular, the main prerequisite that leads to high-intensity SH motion in the pile vicinity is the redirection of the friction force. As shown in Fig. 12, the circumferential friction is one order of magnitude higher (or even more) than the vertical component for the majority of pile installation. Therefore, the mechanism of friction redirection is not solely associated with advantageous installation performance, but also with an induced localized medium disturbance, particularly for the case of SH motion characterized by high frequency (and thus small wavelengths). It is remarked that due to the coupling of the friction components (Eqs. (29) and (30)), both SV-P and SH

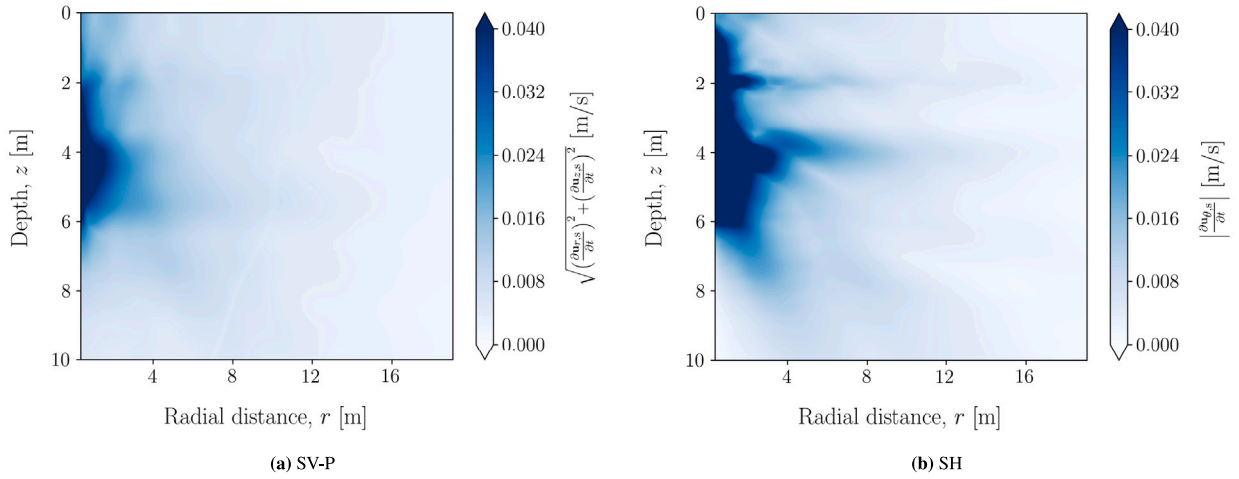


**(a)** SV-P **(b)** SH

**Fig. 14.** Comparison of PPVs associated with (a) the SV-P wavefield and (b) the SH wavefield, for $GDP_1$ and at $u_R = 5.5$ m.

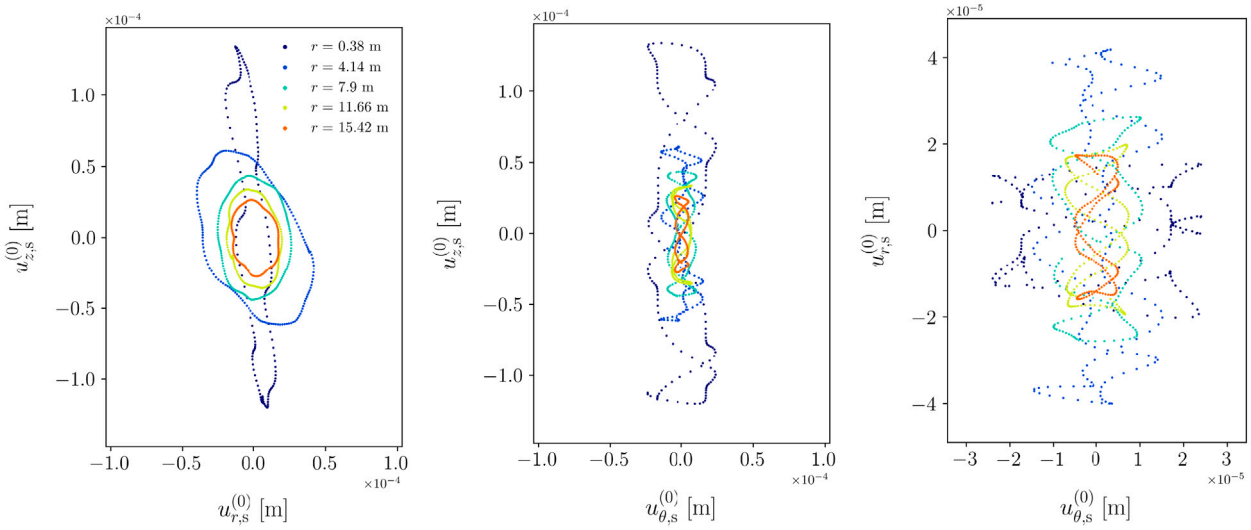


**(a)** **(b)** **(c)**

**Fig. 15.** Trajectories of soil particle motion at various receiver radii on the ground surface and for $u_R = 5.5$ m.

wavefields are characterized by rich frequency content; this is also testified by the vertical friction forces in Fig. 9 eliciting the SV-P wavefield, as well as the SV-P particle trajectories in Fig. 15. The axial-torsional excitation and the frictional coupling effectively result into redistribution of the energy throughout the frequency spectrum at the interaction harmonics (see Eq. (38)). Naturally, an extensive parametric study of combined numerical and experimental character is deemed necessary to identify the admissible parameter space for the amplitudes and frequencies of the axial-torsional excitation, with a view to successful application of GDP.

## 6. Conclusions

In this paper, a numerical model for the analysis of pile installation via GDP was presented and utilized to decipher the mechanics of this novel driving technique. Specifically, the GDP model builds on a recently developed numerical framework for axial vibratory driving, with main extensions the increase of the degrees-of-freedom (DoFs) (due to the addition of circumferential motion) and the application of the AHBM (due to the relation of the driving frequencies). As regards the soil reaction, the SCPT-based formulation from vibratory driving was employed as an initial basis. Upon modification of the tip reaction, the adopted set of parameters led to GDP model predictions that compared favourably with field data from the GDP campaign. Therefore, a unified modelling framework that is suitable to analyse pile installation via axial vibratory and GDP methods has been realized. Conclusively, the main observations and findings pertaining to the study of the pile installation process via GDP are summarized as follows:

– a unified modelling framework was presented and benchmarked with field data for the analysis of axial vibro-driving and GDP.

– the friction force at the pile–soil interface was predominantly expended in the circumferential direction. The redirection of the friction force vector emerges as the main driving mechanism in GDP, that leads to enhanced installation performance.

– as a consequence of the previous point, the majority of the power dissipation through the soil reaction corresponds to the circumferential friction. This finding also implies a dissimilar soil response compared to standard vibro-driving.

– the soil motion during pile installation via GDP elicits both SH and SV-P waves, with the former wavefield being dominant. This result encourages further experiments to investigate the potential abatement of the SV-P wavefield in GDP.

– SV-P motion appears to surpass the respective SH component at the ground surface and with increasing distance, owing to the faster

decay of the high-frequency waves induced by torsion. Therefore, the Rayleigh waves may still comprise the main environmental disturbance in large distances from the source, albeit significantly abated.

## CRediT authorship contribution statement

**Athanasios Tsetas:** Conceptualization, Methodology, Software, Validation, Formal analysis, Investigation, Data curation, Visualization, Writing – original draft. **Apostolos Tsouvalas:** Conceptualization, Methodology, Writing – review & editing, Supervision, Project administration, Funding acquisition. **Andrei V. Metrikine:** Conceptualization, Methodology, Writing – review & editing, Supervision, Project administration, Funding acquisition.

## Declaration of competing interest

The authors declare that they have no known competing financial interests or personal relationships that could have appeared to influence the work reported in this paper.

## Data availability

The authors do not have permission to share data.

## Acknowledgments

This paper is associated with the GDP project in the framework of the GROW joint research programme. Funding from *Topsector Energiesubsidie van het Ministerie van Economische Zaken* under grant number TEHE117100 and financial/technical support from the following partners is gratefully acknowledged: Royal Boskalis Westminster N.V., CAPE Holland B.V., Deltares, Delft Offshore Turbine B.V., Delft University of Technology, ECN, Eneco Wind B.V., IHC IQIP B.V., RWE Offshore Wind Netherlands B.V., SHL Offshore Contractors B.V., Shell Global Solutions International B.V., Sif Netherlands B.V., TNO, and Van Oord Offshore Wind Projects B.V.

## Appendix A. Vibrations of cylindrical shells via the SAFE method

The SAFE mass and stiffness matrices $\mathbf{I}^{\mathrm{s},l}_{\mathrm{p},0}$ and $\mathbf{L}^{\mathrm{s},l}_{\mathrm{p},0}$ for the axial–radial motion (i.e. $n = 0$ and symmetric configuration) of a cylindrical shell segment $l$ with length $d_l$ read as in Eqs. (A.1) and (A.2) (see Box I), where $D_{\mathrm{p}} = \frac{E_{\mathrm{p}} h_{\mathrm{p}}}{1-\nu_{\mathrm{p}}^2}$.

Similarly, for the torsional motion (i.e. $n = 0$ and anti-symmetric configuration) the SAFE mass and stiffness matrices $\mathbf{I}^{\mathrm{a},l}_{\mathrm{p},0}$ and $\mathbf{L}^{\mathrm{a},l}_{\mathrm{p},0}$ are defined as:

$$\mathbf{I}^{\mathrm{a},l}_{\mathrm{p},0} = 2\pi R_{\mathrm{p}} h_{\mathrm{p}} \rho_{\mathrm{p}} \begin{bmatrix} \frac{d_l}{3} & \frac{d_l}{6} \\ \frac{d_l}{6} & \frac{d_l}{3} \end{bmatrix} \tag{A.3}$$

$$\mathbf{L}^{\mathrm{a},l}_{\mathrm{p},0} = 2\pi R_{\mathrm{p}} D_{\mathrm{p}} \begin{bmatrix} \frac{\left(6R_{\mathrm{p}}^2+h_{\mathrm{p}}^2\right)(1-\nu_{\mathrm{p}})}{12R_{\mathrm{p}}^2 d_l} & -\frac{\left(6R_{\mathrm{p}}^2+h_{\mathrm{p}}^2\right)(1-\nu_{\mathrm{p}})}{12R_{\mathrm{p}}^2 d_l} \\ -\frac{\left(6R_{\mathrm{p}}^2+h_{\mathrm{p}}^2\right)(1-\nu_{\mathrm{p}})}{12R_{\mathrm{p}}^2 d_l} & \frac{\left(6R_{\mathrm{p}}^2+h_{\mathrm{p}}^2\right)(1-\nu_{\mathrm{p}})}{12R_{\mathrm{p}}^2 d_l} \end{bmatrix} \tag{A.4}$$

We proceed to showcase the incorporation of hysteretic damping in the pile equations of motion. It is known that hysteretic damping can be formulated in the frequency domain and cannot be transposed in the time domain (Géradin and Rixen, 2014). However, in our problem the periodic response of the system is computed in certain states; by virtue of this periodicity the transformation from time to frequency domain (and vice versa) is trivial. Consider the equilibrium equations of the pile generalized coordinates for the axial–radial motion (Eq. (10)) upon transformation to the frequency domain, including hysteretic damping:

$$-\omega^2 \mathbf{I}_{N_m} \widetilde{\mathbf{q}}^{\mathrm{s}}_0 + \left(1 + 2\mathrm{i}\xi_{\mathrm{p}} \mathrm{sgn}(\omega)\right) \boldsymbol{\Omega}^2 \widetilde{\mathbf{q}}^{\mathrm{s}}_0 = \left(\boldsymbol{\Phi}^{\mathrm{s}}_{\mathrm{p},0}\right)^{\mathrm{T}} \widetilde{\mathbf{p}^{\mathrm{s}}_{\mathrm{p},0}} \tag{A.5}$$

where the orthogonality relationships have been normalized as follows:

$$\left(\boldsymbol{\Phi}^{\mathrm{s}}_{\mathrm{p},0}\right)^{\mathrm{T}} \mathbf{I}^{\mathrm{s}}_{\mathrm{p},0} \boldsymbol{\Phi}^{\mathrm{s}}_{\mathrm{p},0} = \mathbf{I}_{N_m}, \quad \left(\boldsymbol{\Phi}^{\mathrm{s}}_{\mathrm{p},0}\right)^{\mathrm{T}} \mathbf{L}^{\mathrm{s}}_{\mathrm{p},0} \boldsymbol{\Phi}^{\mathrm{s}}_{\mathrm{p},0} = \boldsymbol{\Omega}^2 \tag{A.6}$$

where $\mathbf{I}_{N_m}$ is the $N_m \times N_m$ identity matrix, $\boldsymbol{\Omega} = \mathrm{diag}\left\{\omega^{\mathrm{s}}_{0,1} \;\; \omega^{\mathrm{s}}_{0,2} \;\; \cdots\right\}$ is a diagonal matrix with $\omega^{\mathrm{s}}_{0,\mathrm{m}}$ denoting the natural frequency of the $m$–th axial–radial shell mode *in vacuo*. In Eq. (A.5), the hysteretic damping has been introduced in the form of complex Young's modulus, i.e. $E^*_{\mathrm{p}} = E_{\mathrm{p}}(1 + 2\mathrm{i}\xi_{\mathrm{p}}\mathrm{sgn}(\omega))$, thus being a multiplier of the term arising from the SAFE stiffness matrix.

The generalized coordinates $\mathbf{q}^{\mathrm{s}}_0$ (Eq. (39)) can be expressed compactly as:

$$\mathbf{q}^{\mathrm{s}}_0 = \mathbf{h}_0 + \mathbf{C}^{\mathrm{s}}_c \mathbf{h}_c + \mathbf{C}^{\mathrm{s}}_s \mathbf{h}_s \tag{A.7}$$

where the coefficient matrices $\mathbf{C}^{\mathrm{s}}_c$, $\mathbf{C}^{\mathrm{s}}_s$ and the Fourier vectors $\mathbf{h}_0$, $\mathbf{h}_c$, $\mathbf{h}_s$ are defined as follows:

$$\mathbf{C}^{\mathrm{s}}_c = \begin{bmatrix} c^{\mathrm{s}}_{1,1} & c^{\mathrm{s}}_{1,2} & \cdots \\ c^{\mathrm{s}}_{2,1} & c^{\mathrm{s}}_{2,2} & \cdots \\ \vdots & \vdots & \ddots \end{bmatrix}^{\mathrm{T}} \tag{A.8}$$

$$\mathbf{C}^{\mathrm{s}}_s = \begin{bmatrix} s^{\mathrm{s}}_{1,1} & s^{\mathrm{s}}_{1,2} & \cdots \\ s^{\mathrm{s}}_{2,1} & s^{\mathrm{s}}_{2,2} & \cdots \\ \vdots & \vdots & \ddots \end{bmatrix}^{\mathrm{T}} \tag{A.9}$$

$$\mathbf{h}_0 = \begin{bmatrix} c^{\mathrm{s}}_{1,0} & c^{\mathrm{s}}_{2,0} & \cdots \end{bmatrix}^{\mathrm{T}} \tag{A.10}$$

$$\mathbf{h}_c = \begin{bmatrix} \cos(j_1 \Omega_0 t) & \cos(j_2 \Omega_0 t) & \cdots \end{bmatrix}^{\mathrm{T}} \tag{A.11}$$

$$\mathbf{h}_s = \begin{bmatrix} \sin(j_1 \Omega_0 t) & \sin(j_2 \Omega_0 t) & \cdots \end{bmatrix}^{\mathrm{T}} \tag{A.12}$$

where the Fourier coefficients $c^{\mathrm{s}}_{0,j}$ and $s^{\mathrm{s}}_{0,j}$ associated with the $m$–th axial–radial mode have been defined in Eq. (39) and $j_1$, $j_2$ are members of the set $S_0$.

By virtue of the periodic generalized coordinates (Eq. (A.7)), the transformation of Eq. (A.5) to the time domain can be readily obtained as follows:

$$\begin{aligned} &-\Omega_0^2 \left(\mathbf{C}^{\mathrm{s}}_c \mathbf{J}^2 \mathbf{h}_c + \mathbf{C}^{\mathrm{s}}_s \mathbf{J}^2 \mathbf{h}_s\right) + 2\xi_{\mathrm{p}} \boldsymbol{\Omega}^2 \left(\mathbf{C}^{\mathrm{s}}_s \mathbf{h}_c - \mathbf{C}^{\mathrm{s}}_c \mathbf{h}_s\right) \\ &+ \boldsymbol{\Omega}^2 \left(\mathbf{h}_0 + \mathbf{C}^{\mathrm{s}}_c \mathbf{h}_c + \mathbf{C}^{\mathrm{s}}_s \mathbf{h}_s\right) = \left(\boldsymbol{\Phi}^{\mathrm{s}}_{\mathrm{p},0}\right)^{\mathrm{T}} \mathbf{p}^{\mathrm{s}}_{\mathrm{p},0} \end{aligned} \tag{A.13}$$

where $\mathbf{J} = \mathrm{diag}\left\{j_1 \;\; j_2 \;\; \cdots\right\}$.

As can be seen, Eq. (A.13) can be directly substituted in Eq. (44d) to account for hysteretic damping. The exact same procedure can be employed for the axisymmetric torsional motion associated with $\mathbf{q}^{\mathrm{a}}_0$. It is noted that the preceding treatment includes only the flexible body modes ($m > 0$), as energy dissipation due to material hysteresis does not take place during rigid body motion ($m = 0$), i.e. the structure translates/rotates as a rigid body without deformation.

## Appendix B. Thin-layer matrices for linear elastic isotropic media

For the case of linear Lagrange polynomials used as interpolation functions, the TLM matrices read:

$$\mathbf{A}^l = \left(1 + 2\mathrm{i}\xi_{\mathrm{s}} \mathrm{sgn}(\omega)\right) \frac{h_l}{6} \begin{bmatrix} 2(\lambda_{\mathrm{s}} + 2G_{\mathrm{s}}) & 0 & 0 & \lambda_{\mathrm{s}} + 2G_{\mathrm{s}} & 0 & 0 \\ 0 & 2G_{\mathrm{s}} & 0 & 0 & G_{\mathrm{s}} & 0 \\ 0 & 0 & 2G_{\mathrm{s}} & 0 & 0 & G_{\mathrm{s}} \\ \lambda_{\mathrm{s}} + 2G_{\mathrm{s}} & 0 & 0 & 2(\lambda_{\mathrm{s}} + 2G_{\mathrm{s}}) & 0 & 0 \\ 0 & G_{\mathrm{s}} & 0 & 0 & 2G_{\mathrm{s}} & 0 \\ 0 & 0 & G_{\mathrm{s}} & 0 & 0 & 2G_{\mathrm{s}} \end{bmatrix} \tag{B.1}$$

$$\mathbf{I}^{s,l}_{\mathrm{p},0} = 2\pi R_{\mathrm{p}} h_{\mathrm{p}} \rho_{\mathrm{p}} \begin{bmatrix} \frac{d_l}{3} & 0 & 0 & \frac{d_l}{6} & 0 & 0 \\ 0 & \frac{13d_l}{35} & \frac{11d_l^2}{210} & 0 & \frac{9d_l}{70} & -\frac{13d_l^2}{420} \\ 0 & \frac{11d_l^2}{210} & \frac{d_l^3}{105} & 0 & \frac{13d_l^2}{420} & -\frac{d_l^3}{140} \\ \frac{d_l}{6} & 0 & 0 & \frac{d_l}{3} & 0 & 0 \\ 0 & \frac{9d_l}{70} & \frac{13d_l^2}{420} & 0 & \frac{13d_l}{35} & -\frac{11d_l^2}{210} \\ 0 & -\frac{13d_l^2}{420} & -\frac{d_l^3}{140} & 0 & -\frac{11d_l^2}{210} & \frac{d_l^3}{105} \end{bmatrix} \tag{A.1}$$

$$\mathbf{L}^{s,l}_{\mathrm{p},0} = 2\pi R_{\mathrm{p}} D_{\mathrm{p}} \begin{bmatrix} \frac{1}{d_l} & -\frac{\nu_{\mathrm{p}}}{2R_{\mathrm{p}}} & -\frac{d_l\nu_{\mathrm{p}}}{12R_{\mathrm{p}}} & -\frac{1}{d_l} & -\frac{\nu_{\mathrm{p}}}{2R_{\mathrm{p}}} & \frac{d_l\nu_{\mathrm{p}}}{12R_{\mathrm{p}}} \\ -\frac{\nu_{\mathrm{p}}}{2R_{\mathrm{p}}} & \frac{35h_{\mathrm{p}}^2R_{\mathrm{p}}^2+13d_l^4}{35d_l^3R_{\mathrm{p}}^2} & \frac{105h_{\mathrm{p}}^2R_{\mathrm{p}}^2+11d_l^4}{210d_l^2R_{\mathrm{p}}^2} & \frac{\nu_{\mathrm{p}}}{2R_{\mathrm{p}}} & \frac{-70h_{\mathrm{p}}^2R_{\mathrm{p}}^2+9d_l^4}{70d_l^3R_{\mathrm{p}}^2} & \frac{210h_{\mathrm{p}}^2R_{\mathrm{p}}^2-13d_l^4}{420d_l^2R_{\mathrm{p}}^2} \\ -\frac{d_l\nu_{\mathrm{p}}}{12R_{\mathrm{p}}} & \frac{105h_{\mathrm{p}}^2R_{\mathrm{p}}^2+11d_l^4}{210d_l^2R_{\mathrm{p}}^2} & \frac{35h_{\mathrm{p}}^2R_{\mathrm{p}}^2+d_l^4}{105d_lR_{\mathrm{p}}^2} & \frac{d_l\nu_{\mathrm{p}}}{12R_{\mathrm{p}}} & \frac{-210h_{\mathrm{p}}^2R_{\mathrm{p}}^2+13d_l^4}{420d_l^2R_{\mathrm{p}}^2} & \frac{70h_{\mathrm{p}}{}^2R_{\mathrm{p}}{}^2-3d_l^4}{420d_lR_{\mathrm{p}}{}^2} \\ -\frac{1}{d_l} & \frac{\nu_{\mathrm{p}}}{2R_{\mathrm{p}}} & \frac{d_l\nu_{\mathrm{p}}}{12R_{\mathrm{p}}} & \frac{1}{d_l} & \frac{\nu_{\mathrm{p}}}{2R_{\mathrm{p}}} & -\frac{d_l\nu_{\mathrm{p}}}{12R_{\mathrm{p}}} \\ -\frac{\nu_{\mathrm{p}}}{2R_{\mathrm{p}}} & \frac{-70h_{\mathrm{p}}{}^2R_{\mathrm{p}}^2+9d_l^4}{70d_l^3R_{\mathrm{p}}^2} & \frac{-210h_{\mathrm{p}}^2R_{\mathrm{p}}^2+13d_l^4}{420d_l^2R_{\mathrm{p}}^2} & \frac{\nu_{\mathrm{p}}}{2R_{\mathrm{p}}} & \frac{35h_{\mathrm{p}}^2R_{\mathrm{p}}^2+13d_l^4}{35d_l^3R_{\mathrm{p}}^2} & \frac{-105h_{\mathrm{p}}^2R_{\mathrm{p}}^2-11d_l^4}{210d_l^2R_{\mathrm{p}}^2} \\ \frac{d_l\nu_{\mathrm{p}}}{12R_{\mathrm{p}}} & \frac{210h_{\mathrm{p}}{}^2R_{\mathrm{p}}^2-13d_l^4}{420d_l^2R_{\mathrm{p}}^2} & \frac{70h_{\mathrm{p}}{}^2R_{\mathrm{p}}^2-3d_l^4}{420d_lR_{\mathrm{p}}^2} & -\frac{h_{\mathrm{p}}\nu_{\mathrm{p}}}{12R_{\mathrm{p}}} & \frac{-105h_{\mathrm{p}}{}^2R_{\mathrm{p}}^2-11d_l^4}{210d_l^2R_{\mathrm{p}}^2} & \frac{35h_{\mathrm{p}}^2R_{\mathrm{p}}^2+d_l^4}{105d_lR_{\mathrm{p}}^2} \end{bmatrix} \tag{A.2}$$

**Box I.**

$$\mathbf{B}^l = \frac{\left(1+2\mathrm{i}\xi_{\mathrm{s}}\mathrm{sgn}(\omega)\right)}{2} \begin{bmatrix} 0 & 0 & -G_{\mathrm{s}}+\lambda_{\mathrm{s}} & 0 & 0 & -G_{\mathrm{s}}-\lambda_{\mathrm{s}} \\ 0 & 0 & 0 & 0 & 0 & 0 \\ -G_{\mathrm{s}}+\lambda_{\mathrm{s}} & 0 & 0 & G_{\mathrm{s}}+\lambda_{\mathrm{s}} & 0 & 0 \\ 0 & 0 & G_{\mathrm{s}}+\lambda_{\mathrm{s}} & 0 & 0 & G_{\mathrm{s}}-\lambda_{\mathrm{s}} \\ 0 & 0 & 0 & 0 & 0 & 0 \\ -G_{\mathrm{s}}-\lambda_{\mathrm{s}} & 0 & 0 & G_{\mathrm{s}}-\lambda_{\mathrm{s}} & 0 & 0 \end{bmatrix} \tag{B.2}$$

$$\mathbf{G}^l = \frac{\left(1+2\mathrm{i}\xi_{\mathrm{s}}\mathrm{sgn}(\omega)\right)}{h_l} \begin{bmatrix} G_{\mathrm{s}} & 0 & 0 & -G_{\mathrm{s}} & 0 & 0 \\ 0 & G_{\mathrm{s}} & 0 & 0 & -G_{\mathrm{s}} & 0 \\ 0 & 0 & \lambda_{\mathrm{s}}+2G_{\mathrm{s}} & 0 & 0 & -\lambda_{\mathrm{s}}-2G_{\mathrm{s}} \\ -G_{\mathrm{s}} & 0 & 0 & G_{\mathrm{s}} & 0 & 0 \\ 0 & -G_{\mathrm{s}} & 0 & 0 & G_{\mathrm{s}} & 0 \\ 0 & 0 & -\lambda_{\mathrm{s}}-2G_{\mathrm{s}} & 0 & 0 & \lambda_{\mathrm{s}}+2G_{\mathrm{s}} \end{bmatrix} \tag{B.3}$$

$$\mathbf{M}^l = \frac{\rho_{\mathrm{s}} h_l}{6} \begin{bmatrix} 2 & 0 & 0 & 1 & 0 & 0 \\ 0 & 2 & 0 & 0 & 1 & 0 \\ 0 & 0 & 2 & 0 & 0 & 1 \\ 1 & 0 & 0 & 2 & 0 & 0 \\ 0 & 1 & 0 & 0 & 2 & 0 \\ 0 & 0 & 1 & 0 & 0 & 2 \end{bmatrix} \tag{B.4}$$

The matrices $\mathbf{A}^l$, $\mathbf{B}^l$, $\mathbf{G}^l$ and $\mathbf{M}^l$ characterize each thin layer $l$ (Kausel and Roësset, 1981). By overlapping all the thin layer matrices in the usual FE sense, grouping the DoFs instead of the layer interfaces and rearranging rows and columns, the matrices $\mathbf{A}_r$, $\mathbf{A}_\theta$, $\mathbf{A}_z$, $\mathbf{B}_{zr}$, $\mathbf{B}_{rz}$, $\mathbf{G}_r$, $\mathbf{G}_\theta$, $\mathbf{G}_z$, $\mathbf{M}_r$, $\mathbf{M}_\theta$ and $\mathbf{M}_z$ can be formed, which lead to Eqs. (13) and (14). Finally, hysteretic damping is introduced in the form of complex Lamé parameters, i.e. $\lambda_{\mathrm{s}}^* = \lambda_{\mathrm{s}}(1+2\mathrm{i}\xi_{\mathrm{s}}\mathrm{sgn}(\omega))$ and $G_{\mathrm{s}}^* = G_{\mathrm{s}}(1+2\mathrm{i}\xi_{\mathrm{s}}\mathrm{sgn}(\omega))$. The overall process to obtain the Green's functions is identical, irrespective of the presence of hysteretic damping.

## References


Ahmad, Z., Gabbert, U., 2012. Simulation of lamb wave reflections at plate edges using the semi-analytical finite element method. Ultrasonics 52, 815–820.

Ainslie, M.A., Halvorsen, M.B., Müller, R.A., Lippert, T., 2020. Application of damped cylindrical spreading to assess range to injury threshold for fishes from impact pile driving. J. Acoust. Soc. Am. 148, 108–121.

Aki, K., Richards, P.G., 2002. Quantitative Seismology. University Science Books.

Bandyopadhyay, N., Archer, R.R., 1979. Semi-analytical finite element analysis of end problems for orthotropic cylinders. Int. J. Solids Struct. 15, 871–883.

Barkan, D., 1967. Developments in soil dynamics. In: Proceedings International Symposium on Wave Propagation and Dynamic Properties of Earth Materials. Albuquerque, New Mexico, University of New Mexico Press.

Bilgili, M., Alphan, H., 2022. Global growth in offshore wind turbine technology. Clean Technol. Environ. Policy 24, 2215–2227.

Callahan, J., Baruh, H., 1999. A closed-form solution procedure for circular cylindrical shell vibrations. Int. J. Solids Struct. 36, 2973–3013.

Cameron, T., Griffin, J.H., 1989. An alternating frequency/time domain method for calculating the steady-state response of nonlinear dynamic systems. J. Appl. Mech. 56, 149–154.

De Nicola, A., Randolph, M.F., 1993. Tensile and compressive shaft capacity of piles in sand. J. Geotech. Eng. 119, 1952–1973.

de Oliveira Barbosa, J.M., Park, J., Kausel, E., 2012. Perfectly matched layers in the thin layer method. Comput. Methods Appl. Mech. Engrg. 217, 262–274.

Forsberg, K., 1969. Axisymmetric and beam-type vibrations of thin cylindrical shells. AIAA J. 7, 221–227.

Géradin, M., Rixen, D.J., 2014. Mechanical Vibrations: Theory and Application to Structural Dynamics. John Wiley & Sons.

Gómez, S.S., Tsetas, A., Metrikine, A.V., 2022. Energy flux analysis for quantification of vibratory pile driving efficiency. J. Sound Vib. 541, 117299.

Guo, Y., Wang, H., Lian, J., 2022. Review of integrated installation technologies for offshore wind turbines: Current progress and future development trends. Energy Convers. Manage. 255, 115319.

Guskov, M., Thouverez, F., 2012. Harmonic balance-based approach for quasi-periodic motions and stability analysis. J. Vib. Acoust. 134.

International Energy Agency, 2022. World Energy Outlook 2022. Technical Report, Paris, France.

Jensen, F.B., Kuperman, W.A., Porter, M.B., Schmidt, H., Tolstoy, A., 2011. Computational Ocean Acoustics, Vol. 794. Springer.

Juhász, Z., Szekrényes, A., 2015. Progressive buckling of a simply supported de-laminated orthotropic rectangular composite plate. Int. J. Solids Struct. 69, 217–229.

Kausel, E., 1981. An Explicit Solution for the Green Functions for Dynamic Loads in Layered Media. Technical Report R81-13, Publication No. 699, Department of Civil Engineering, Massachusetts Institute of Technology.

Kausel, E., 1999. Dynamic point sources in laminated media via the thin-layer method. Int. J. Solids Struct. 36, 4725–4742.
Kausel, E., 2006. Fundamental Solutions in Elastodynamics: A Compendium. Cambridge University Press.
Kausel, E., de Oliveira Barbosa, J.M., 2012. PMLs: A direct approach. Internat. J. Numer. Methods Engrg. 90, 343–352.
Kausel, E., Peek, R., 1982. Dynamic loads in the interior of a layered stratum: an explicit solution. Bull. Seismol. Soc. Am. 72, 1459–1481.
Kausel, E., Roësset, J.M., 1981. Stiffness matrices for layered soils. Bull. Seismol. Soc. Am. 71, 1743–1761.
Kaynia, A.M., Hebig, J., Pein, T., Shin, Y., 2022. Numerical model for dynamic installation of large diameter monopiles. Soil Dyn. Earthq. Eng. 161, 107393.
Kementzetzidis, E., Pisanò, F., Elkadi, A., Tsouvalas, A., Metrikine, A., 2023a. Gentle driving of piles (GDP) at a sandy site combining axial and torsional vibrations: Part II - cyclic/dynamic lateral loading tests. Ocean Eng. 270, 113452.
Kementzetzidis, E., Pisanò, F., Tsetas, A., Metrikine, A., 2023b. Gentle driving of piles (GDP) at a sandy site combining axial and torsional vibrations: quantifying the influence of pile installation method on lateral behaviour. J. Geoenviron. Geotech. Eng..
Krack, M., Gross, J., 2019. Harmonic Balance for Nonlinear Vibration Problems, Vol. 1. Springer.
Kucukcoban, S., Goh, H., Kallivokas, L.F., 2019. On the full-waveform inversion of lamé parameters in semi-infinite solids in plane strain. Int. J. Solids Struct. 164, 104–119.
Love, A.E.H., 1888. XVI. The small free vibrations and deformation of a thin elastic shell. Philos. Trans. R. Soc. Lond. A 179, 491–546.
Love, A.E.H., 1944. A Treatise on the Mathematical Theory of Elasticity. Dover Publications.
Machaček, J., Staubach, P., Tafili, M., Zachert, H., Wichtmann, T., 2021. Investigation of three sophisticated constitutive soil models: From numerical formulations to element tests and the analysis of vibratory pile driving tests. Comput. Geotech. 138, 104276.
Masoumi, H., Degrande, G., Lombaert, G., 2007. Prediction of free field vibrations due to pile driving using a dynamic soil–structure interaction formulation. Soil Dyn. Earthq. Eng. 27, 126–143.
Masoumi, H.R., François, S., Degrande, G., 2009. A non-linear coupled finite element–boundary element model for the prediction of vibrations due to vibratory and impact pile driving. Int. J. Numer. Anal. Methods Geomech. 33, 245–274.
Mazza, N., Holeyman, A., 2019. Frequency-penetration response spectrum on vibratory amplitude matching of monopiles. In: 10th International Conference on Stress Wave Theory and Testing Methods for Deep Foundations. ASTM International.
Merchant, N.D., 2019. Underwater noise abatement: economic factors and policy options. Environ. Sci. Policy 92, 116–123.
Moriyasu, S., Kobayashi, S., Matsumoto, T., 2018. Experimental study on friction fatigue of vibratory driven piles by in situ model tests. Soils Found. 58, 853–865.
Musial, W., Spitsen, P., Duffy, P., Beiter, P., Marquis, M., Hammond, R., Shields, M., 2022. Offshore Wind Market Report: 2022 Edition. Technical Report, National Renewable Energy Lab.(NREL), Golden, CO (United States).
Nguyen, C.T., Tassoulas, J.L., 2018. Reciprocal absorbing boundary condition with perfectly matched discrete layers for transient analysis of sv-p waves in a layered half-space. Int. J. Solids Struct. 155, 89–108.
Quaegebeur, S., Chouvion, B., Thouverez, F., 2022. Nonlinear dynamic analysis of three-dimensional bladed-disks with frictional contact interfaces based on cyclic reduction strategies. Int. J. Solids Struct. 236, 111277.
Ramírez, L., Fraile, D., Brindley, G., 2021. Offshore Wind in Europe: Key Trends and Statistics 2020. WindEurope.
Rodger, A., Littlejohn, G., 1980. A study of vibratory driving in granular soils. Géotechnique 30, 269–293.
Sheng, D., Eigenbrod, K.D., Wriggers, P., 2005. Finite element analysis of pile installation using large-slip frictional contact. Comput. Geotech. 32, 17–26.
Staubach, P., Machaček, J., Skowronek, J., Wichtmann, T., 2021. Vibratory pile driving in water-saturated sand: Back-analysis of model tests using a hydro-mechanically coupled cel method. Soils Found. 61, 144–159.
Taciroglu, E., Liu, C., Dong, S., Chun, C., 2004. Analysis of laminated piezoelectric circular cylinders under axisymmetric mechanical and electrical loads with a semi-analytic finite element method. Int. J. Solids Struct. 41, 5185–5208.
Timoshenko, S.P., Woinowsky-Krieger, S., 1959. Theory of Plates and Shells. McGraw-hill.
Tsetas, A., 2023. A Unified Modelling Framework for Vibratory Pile Driving Methods (Ph.D. thesis). Delft University of Technology.
Tsetas, A., Gómez, S.S., Tsouvalas, A., van Beek, K., Tehrani, F.S., Kementzetzidis, E., Pisanò, F., Elkadi, A., Segeren, M., Molenkamp, T., Metrikine, A.V., 2020. Experimental identification of the dynamic behaviour of pile-soil system installed by means of three different pile-driving techniques. In: Proceedings of the XI International Conference on Structural Dynamics, EURODYN 2020, Volume II. European Association for Structural Dynamics, pp. 3005–3015.
Tsetas, A., Tsouvalas, A., Gómez, S., Pisanò, F., Kementzetzidis, E., Molenkamp, T., Elkadi, A., Metrikine, A., 2023a. Gentle driving of piles (GDP) at a sandy site combining axial and torsional vibrations: Part I - installation tests. Ocean Eng. 270, 113453.
Tsetas, A., Tsouvalas, A., Metrikine, A.V., 2021. Installation of large-diameter monopiles: introducing wave dispersion and non-local soil reaction. J. Mar. Sci. Eng. 9, 313.
Tsetas, A., Tsouvalas, A., Metrikine, A.V., 2022. An alternating frequency-time harmonic balance method for fast-slow dynamical systems. In: Proceedings of the 28th International Congress on Sound and Vibration, Vol. IIAV. International Institute of Acoustics and Vibration.
Tsetas, A., Tsouvalas, A., Metrikine, A.V., 2023b. A non-linear three-dimensional pile–soil model for vibratory pile installation in layered media. Int. J. Solids Struct. 269, 112202. http://dx.doi.org/10.1016/j.ijsolstr.2023.112202.
Tsouvalas, A., 2020. Underwater noise emission due to offshore pile installation: A review. Energies 13, 3037.
Tsouvalas, A., Metrikine, A.V., 2016. Structure-borne wave radiation by impact and vibratory piling in offshore installations: From sound prediction to auditory damage. J. Mar. Sci. Eng. 4, 44.
White, D., Lehane, B., 2004. Friction fatigue on displacement piles in sand. Géotechnique 54, 645–658.
Williams, R., Zhao, F., Lee, J., 2022. Global Offshore Wind Report 2022. Technical Report, Global Wind Energy Council, Brussels, Belgium.
Xiao, Y., Ge, Y., 2022. A numerical model of vps for offshore wind turbine monopiles based on hypoplastic theory. Int. J. Numer. Anal. Methods Geomech. 46, 697–716.
Zhou, S., Cao, J., Inman, D.J., Lin, J., Li, D., 2016. Harmonic balance analysis of nonlinear tristable energy harvesters for performance enhancement. J. Sound Vib. 373, 223–235.